7. Monte Carlo Techniques for Quantum Fluids, Solids and Droplets

Kevin E. Schmidt and David M. Ceperley

With 12 Figures

In this chapter we review the progress that has been made since the publication of the previous articles [7.1, 2] hereafter referred to as I and II. The major advances not covered in those two reviews are improved variational wavefunctions, path integral methods for calculating at temperatures $T > 0$, systems with interfaces such as surfaces and droplets, and the calculation of exchange frequencies in quantum crystals. We will concentrate on these areas and on the Monte Carlo techniques used. We will give results from some representative calculations.

The principle constituents of the systems we describe are the helium isotopes ^{3}He and ^{4}He. Other many-body quantum systems such as electron systems, polarised hydrogen and its isotopes, can be handled in a similar way. Systems with spin and/or isospin dependent forces like nuclei are much more difficult and require nontrivial generalisations of the techniques presented here, and are beyond the scope of this work. The interested reader is referred to the recent work by *Pieper* et al. [7.3] and *Carlson* [7.4, 5] for some current Monte Carlo attacks on the nuclear structure problem.

The Hamiltonian we consider is

$$H = -\frac{1}{2m}\sum_{i=1}^{N}\nabla_i^2 + \sum_{i<j} v_{ij}, \tag{7.1}$$

with obvious generalisations to mixtures, substrates, three-body potentials, etc. We set $\hbar = 1$, m is the mass, and $v_{ij} = v(|\boldsymbol{r}_i - \boldsymbol{r}_j|)$ is the pair potential. Throughout this work we denote the $3N$ coordinates of the N atoms by R.

We will describe, in Sect. 7.1 some wavefunctions used currently in variational studies. These include 3-body and backflow correlations in addition to the standard Bijl–Dingle–Jastrow form of the many-body wavefunction; the pairing forms for the wavefunction developed by *Bouchaud* and *Lhuillier* [7.6]; and the shadow wavefunctions of *Vitiello* et al. [7.7]. We will also discuss some useful optimisation methods. In Sect. 7.2, we will define the Green's functions Monte Carlo (GFMC) method and briefly discuss some fermion methods. The path integral Monte Carlo (PIMC) method, which has been developed and applied since I and II were published, will be described in Sect. 7.3. We will give some results of calculations of helium bulk properties in Sect. 7.4, and momentum distributions and related density matrices in Sect. 7.5. In Sect. 7.6, we will give an introduction to some work on droplets, and Sect. 7.7 give some possible future directions for Monte Carlo simulations of quantum fluids.

Techniques other than Monte Carlo simulations have made important contributions to the understanding of many systems and particularly in the development of good variational wavefunctions. However, we will only refer to these methods when they have a direct bearing on the Monte Carlo development.

Some systematic errors are common to all of the Monte Carlo calculations we describe. These include the interaction potential, size dependence, statistical errors, convergence problems and bias.

The 2-body HFDHE2 potential of *Aziz* et al. [7.8] has become the potential of choice for helium studies in part because of the good agreement between GFMC ground-state calculations and the experimental low-temperature equation of state for ^{4}He. The potential needs to be revised by softening the core [7.9, 10] and Aziz and coworkers have published a new He–He potential [7.11]. The attractive well may have to be deepened somewhat [7.11, 12], although the evidence here is much less compelling, and the HFDHE2 well depth is within estimated theoretical bounds. In any case, the HFDHE2 potential is accurate to better than 0.2 K per particle out of the 20 K potential energy in ^{4}He at equilibrium density. Three-body potential effects are not well characterised, but estimates [7.13], mostly based on the Axilrod–Teller interaction [7.14], show that they are also in this range. Work at much higher pressures will require a better understanding of these 3-body forces. Recent attempts to calculate, using the Monte Carlo method, the 2- and 3-body helium interaction potentials have been successful in the highly repulsive region [7.9], but have not been conclusive in the region of the attractive well because the statistical errors have been of order 0.1 K [7.15–17].

Size dependence of the ground state energy and local properties of bulk ^{4}He are small as stated in I. However, the momentum distribution as usually calculated, has the incorrect behaviour at long wavelength [7.18], and the specific heat curve is rounded around the lambda transition [7.19]. These are a direct consequence of the finite size of the simulations used. As we shall see in Sect. 7.3, PIMC calculations which need to sample paths with a change in the winding number, are currently limited to small systems (100 atoms). In the fermi system ^{3}He, shell effects due to the very nonspherical fermi surface can be quite large [7.20, 21], of order 0.1 K per particle even for N over 100. These will make difficult the extraction from Monte Carlo calculations of a number of interesting properties such as the spin susceptibility and the effective mass.

Statistical errors, lack of convergence, and bias of the Monte Carlo calculations can also be a major problem; witness the GFMC density profiles calculated for droplets [7.22, 23] and for the free surface [7.24]. Here the slow convergence makes difficult the calculation of the exact ground-state density from the variational and GFMC mixed estimates. Clearly, the extrapolation from the variational and GFMC mixed estimates described in I and II should only be trusted when variational and mixed estimates are close so that the neglected second order error term can be assumed small. An advantage of PIMC over GFMC is that this extrapolation is not needed. A possible combination of GFMC and PIMC can be made by replacing the closed path

by a path which ends with a good variational trial wave function. The resulting method would combine, for zero temperature problems, some of the advantages and disadvantages of the GFMC, PIMC and shadow wavefunction methods.

Great care needs to be taken in all Monte Carlo calculations to eliminate the effects of bias, autocorrelation, and lack of convergence. Much of the advice given by *Binder*, *Stauffer* and *Heermann* [7.25,26] can be applied directly to quantum simulations.

7.1 Variational Method

7.1.1 Variational Wavefunctions

The variational Monte Carlo method and its application to both Bose and Fermi systems was described in I. It consists of calculating the expectation value of operators using the Metropolies Monte Carlo method and an assumed trial wavefunction. Usually the expectation value of the Hamiltonian H is minimised with respect to parameters in the trial wavefunction,

$$E_V = \frac{\int dR \Psi_T(R) H \Psi_T(R)}{\int dR \Psi_T^2(R)} = \langle E_L(R) \rangle \geqq E_0, \tag{7.2}$$

where E_0 is the ground-state energy, $E_L(R)$ is the local energy $H\Psi_T(R)/\Psi_T(R)$, and $P(R) = \Psi_T^2/\int dR \Psi_T^2(R)$ is sampled using the *Metropolis* et al. [7.27] method. A short explanation of the Metropolis method is given in Sect. 7.3, or see I. All expectation values are calculated as averages over $P(R)$ in the variational method.

For bulk ^{3}He and ^{4}He, good trial ground-state variational wavefunctions have been constructed using 2-body, 3-body, and in the case of ^{3}He, backflow [7.28] wavefunctions. The ^{3}He case is less well understood, and in particular, the difficulty in obtaining convincing results for the energy as a function of spin polarisation has lead to the construction of pairing wave functions by *Bouchaud* and *Lhuillier* [7.6]. Similarly, the lack of translational invariance in standard trial solid wavefunctions has recently lead to the introduction of the shadow trial wavefunctions of *Vitiello* et al. [7.7,29]

7.1.2 The Pair Product Wavefunction

The simplest useful trial wavefunction for the ground state of a bulk quantum fluid or solid is the pair product or Bijl–Dingle–Jastrow form,

$$\Psi_T = \prod_{i<j} f_{ij} \Phi, \tag{7.3}$$

usually called the Jastrow form, where Φ is a model, one-body, wavefunction. For the ground state of a Bose liquid, Φ is a constant while for a Fermi liquid it is a Slater determinant of plane waves satisfying periodic boundary conditions.

Table 7.1. Various calculations on liquid ^{4}He at the experimental equilibrium density ($\rho = 0.02186\,\text{A}^{-3}$) using the Aziz HFDHE2 potential and at zero temperature. VMC indicates a variational calculation with the indicated wavefunction. McMillan, PPA, and OPT indicate a Jastrow factor of the McMillan, paired-phonon analysis, or optimized form. 3B indicates the addition of three-body correlations as in (7.5–7). GFMC is done with the McMillan form for the importance and starting function. PIMC is calculated at $T = 1.2\,\text{K}$. n_0 is the fraction of atoms in the zero momentum state

Method	Trial function	Energy	n_0	Reference
VMC	McMillan	−5.72(2)	0.11(1)	[7.88]
VMC	PPA	−5.93(1)	0.107(1)	[7.89]
VMC	Shadow	−6.24(4)	0.045(1)	[7.29]
VMC	McMillan + 3B	−6.65(2)	0.056(1)	[7.89]
VMC	OPT + 3B	−6.79(1)		[7.56]
GFMC	McMillan	−7.12(3)	0.088(5)	[7.88]
PIMC	1.2 K	−7.18(3)	0.080(10)	[7.75]
Experiment	—	−7.14	0.10(3)	[7.36]

Table 7.2. Various calculations on liquid ^{3}He at the experimental equilibrium density ($\rho = 0.01635\,\text{A}^{-3}$) using the Aziz HFDHE2 or the Lennard–Jones potential (marked with *) and at zero temperature. The notation is the same as Table 7.1. Additionally, BF indicates the wavefunction including backflow (7.12), and BCS indicates the pairing wavefunction with singlet ($s = 0$) or triplet ($s = 1$) pairs (7.14, 15). GFMC-FN, GFMC-TE, and GFMC-MP are fixed-node, transient estimation, and mirror potential calculations using the indicated wavefunction

Method	Trial function	Energy	Reference
VMC	McMillan	−1.08(3)	[7.93]
VMC	2B + 3B	−1.61(3)	[7.93]
VMC	2B + BF	−1.55(4)	[7.93]
VMC	2B + 3B + BF	−2.15(3)	[7.21]
VMC	BCS ($s = 0$)*	−1.2	[7.47]
VMC	BCS ($s = 1$)*	−2.05	[7.47]
GFMC-FN	2B + 3B + BF	−2.37(1)	[7.21]
GFMC-MP	2B + 3B + BF	−2.30(4)	[7.21]
GFMC-TE	SB + 3B + BF	−2.44(4)	[7.21]
Experiment	—	−2.47	[7.35]

Since we are dealing with spin-independent forces and operators symmetric under particle interchange, antisymmetry can be enforced by assigning particles a particular spin and antisymmetrising the spatial part under interchange of like spin particles, leading to a determinant for up spins and a determinant for down spins. For quantum solids, Φ is often taken to be the localised form [7.30, 31]

$$\Phi = \exp\left(-C\sum_i |r_i - z_i|^2\right), \tag{7.4}$$

where z_i are assumed lattice positions, and C is a variational parameter. Exchange effects are ignored in this wave function since particles are assigned to specific lattice sites. The solid also loses invariance to simultaneous translation of all the particles, but the wavefunction will give an upper bound to the energy of a Bose solid. The effect of exchange is generally small in 3D solids [7.32]. In practice, including an antisymmetrised or symmetrised form using Monte Carlo sampling is not difficult [7.20, 33].

The results using the simple Jastrow wavefunction, while physically reasonable, are not very accurate as seen in Tables 7.1 and 7.2. For example, the energy of ^{4}He and ^{3}He at the experimental equilibrium density both differ by about 1.2 K from the experimental values of -7.14 K and -2.47 K [7.29, 34–36]. As the densities grow, the Jastrow results become worse.

7.1.3 Three-Body Correlations

The difference between the Jastrow form and the experimental results for ^{4}He is due mainly to the absence of three-body correlations in the trial wavefunctions. An early calculation of model 2D helium was done, using the Monte Carlo method, by *Woo* [7.37]. Later, good variational functions with 3-body correlations were developed using integral equation methods [7.38–40]. The work of Pandharipande was motivated by a correlation operator method, while Chang and Campbell minimised the energy using the convolution approximation. The 3-body correlated wavefunction used in Monte Carlo calculations is similar to these forms, and is [7.41, 42]

$$\Psi_T = \prod_{i<j<k} f^{(3)}_{ijk} \prod_{i<j} f_{ij} \Phi, \tag{7.5}$$

where

$$f^{(3)}_{ijk} = f^{(3)}(r_{ij}, r_{ik}, r_{jk}), \tag{7.6}$$

$$f^{(3)}_{ijk} = \exp\left(\sum_{\text{cyclic}} -\lambda \xi_{ij} \xi_{ik} \boldsymbol{r}_{ij} \cdot \boldsymbol{r}_{ik} \right), \tag{7.7}$$

where λ is a variational parameter, the sum is over cyclic permutations of i, j, and k, and $\xi(r)$ is chosen variationally.

This form can also be motivated by operating on the pair product wavefunction with the Hamiltonian and looking at the local energy, $E_L(R)$ of (7.2). The exact wavefunction must have a constant local energy, so terms which are not constant should be added to the function space of the trial function. The local energy resulting from a pair product trial function has 2-body terms proportional to $\nabla_i^2 f_{ij}/f_{ij}$ or v_{ij}, and 3-body terms like $\nabla_i \log(f_{ij}) \cdot \nabla_i \log(f_{ik})$. Since no choice of a 2-body term $f(r)$ will eliminate the 3-body term, additional 3-body terms must be added to the log of the trial function. These are taken to be $r\xi(r) \approx \nabla \log[f(r)]$ with $\xi(r)$ chosen to minimise the fluctuations in the local energy. A reasonable parameterised choice is simply a Gaussian since the short

range behaviour of ξ is cut off by the repulsive 2-body potential, and the long range behaviour can also be cutoff since it should decay like r^{-4} in 3 dimensions because the long range part of the Jastrow correlation decays like r^{-2} due to zero point phonon excitations.

A nice feature of the 3-body form (7.7) is that it requires only order N^2 operations to calculate instead of order N^3. This can be seen by rewriting the correlation as

$$\prod_{i<j} f_{ij} \prod_{i<j<k} f_{ijk}^{(3)} = \prod_{i<j} \tilde{f}_{ij} \exp\left(-\frac{1}{4}\lambda \sum_l \boldsymbol{G}_l \cdot \boldsymbol{G}_l \right), \tag{7.8}$$

where

$$\boldsymbol{G}_l = \sum_{i \neq l} \xi_{li} \boldsymbol{r}_{li}, \tag{7.9}$$

and

$$\tilde{f}(r) = f(r) \exp\left[\frac{\lambda}{2} \xi^2(r) r^2 \right]. \tag{7.10}$$

If correlations of shorter range than half the size of the simulation cell are used and an average of M particles are within range of the correlation, the 3-body correlations can be calculated in only MN operations.

Usmani et al. [7.43] have used integral equation methods to calculate the effect of a more general 3-body correlation. They included terms with contributions like

$$f_{ijk}^{(3)} = \exp\left[\sum_{\text{cyclic}} \sum_l \lambda_l \xi_{ij}^{(l)} \xi_{ik}^{(l)} P_l(\hat{\boldsymbol{r}}_{ij} \cdot \hat{\boldsymbol{r}}_{ik}) \right], \tag{7.11}$$

where the P_l are Legendre polynomials with $l = 0, 1, 2$ and $\hat{\boldsymbol{r}}$ indicates the unit vector. The $l = 1$ term reduces to the form (7.7). They found that the $l = 0$ term contributes of order 0.1 K in ^{4}He, and the $l = 2$ term is small. Preliminary Monte Carlo calculations agree with these general conclusions. Using the spherical harmonic addition theorem, the Legendre polynomial can be split into a set of $2l + 1$ 2-body sums as in (7.8).

7.1.4 Backflow Correlations

The same arguments used above for the bose system ^{4}He can be applied to motivate 3-body correlations in ^{3}He. For a fermion trial function, the local energy for a pair product trial function includes additional terms proportional to $\nabla_i \log(f_{ij}) \cdot \nabla_i \log(\phi)$, where ϕ is a single-particle orbital in the Slater determinant. Correlations that cancel these terms can be obtained by adding *Feynman–Cohen* [7.28] backflow correlations to the Slater determinant. The backflow form for a liquid, derived by using a beautiful current conservation argument,

is simply a replacement of the orbitals in the Slater determinant,

$$\exp(i\boldsymbol{k}\cdot\boldsymbol{r}_j)\rightarrow\exp\left[i\boldsymbol{k}\cdot\left(\boldsymbol{r}_j+\sum_{m\neq j}\boldsymbol{r}_{jm}\eta_{jm}\right)\right]. \tag{7.12}$$

The argument of the plane wave is simply changed from $\boldsymbol{r}_j$ to $\boldsymbol{r}_j+\sum_{m\neq j}\boldsymbol{r}_{jm}\eta_{jm}$. Feynman and Cohen showed that $\eta(r)\approx r^{-3}$ at large r from hydrodynamic arguments. A similar replacement can be done in inhomogenous systems. For example the orbitals of electrons in molecules should be modified by back flow effects [7.44].

The inclusion of backflow and 3-body correlations has produced very good variational wavefunctions for ^{3}He as judged by the variational energy. A disadvantage of the backflow form is that evaluation of the wave function requires order N^3 operations if $\eta(r)$ is long ranged, even if only one particle is moved at a time. As a consequence, one usually moves all the atoms simultaneously, and to achieve a reasonable acceptance ratio, the step size must be chosen to be small. Often, directed sampling techniques [7.45] are used to improve the efficiency of the Monte Carlo sampling. As in the standard fermion variational Monte Carlo method [see I], the calculation of the derivatives is straightforward. All terms can be calculated using the chain rule and the identity for the determinants of matrices $\boldsymbol{A}$ and $\boldsymbol{B}$,

$$\frac{\det(\boldsymbol{A})}{\det(\boldsymbol{B})}=\det(\boldsymbol{B}^{-1}\boldsymbol{A}). \tag{7.13}$$

7.1.5 Pairing Correlations

Bouchaud and *Lhuillier* [7.6, 46, 47] have developed variational wave functions which contain pairing correlations. In particular, they show that the singlet paired BCS [7.48] wavefunction for N particles can be written as a determinant,

$$\Psi_{\mathrm{BCS}}=\det[\phi(\boldsymbol{r}_{i\mathrm{u}}-\boldsymbol{r}_{j\mathrm{d}})], \tag{7.14}$$

where u and d stand for up and down spin particles, and $\phi(r)$ is the orbital part of the single pair BCS wavefunction. One can show using the properties of Pfaffians [7.49] or Grassman variables that the square of the triplet paired wavefunction is a determinant,

$$\Psi^2_{\mathrm{BCS}}=\det[\phi(\boldsymbol{r}_{i\mathrm{u}}-\boldsymbol{r}_{j\mathrm{u}})]\cdot\det[\phi(\boldsymbol{r}_{i\mathrm{d}}-\boldsymbol{r}_{j\mathrm{d}})]. \tag{7.15}$$

Bouchaud and Lhuillier use these triplet and singlet BCS functions as the model functions in (7.3) with a simple gaussian form for the $\phi(r)$,

$$\phi(r)=\begin{bmatrix}(\hat{\boldsymbol{n}}\cdot\boldsymbol{r})\\ 1\end{bmatrix}\exp\left(\frac{-r}{b}\right)^2, \tag{7.16}$$

where $\hat{\boldsymbol{n}}\cdot\boldsymbol{r}$ goes with the triplet state, 1 with the singlet state, and b is a variational parameter.

Bouchaud and Lhuillier find that the single particle momentum distribution with this pairing form is smooth, with no discontinuity at the fermi momentum in contrast to the distribution resulting from the Slater determinant (see Fig. 7.12, Sect. 7.5). The static structure $S(k)$ is reasonable and close to that calculated with the Slater-determinant [7.47] form owing to the small effect of statistics on the pair correlations in ^{3}He. Results are given in Sects. 7.4 and 7.5.

7.1.6 Shadow Wavefunctions

A new variational wavefunction called the shadow wavefunction has been devised recently by *Vitiello* et al. [7.7]. Their initial motivation was to produce variational wavefunctions for the crystalline phase with the symmetries of the Hamiltonian: translational invariance and particle symmetry. The localised forms assume a particular broken symmetry and thus inhibit studies of the phase transition, vacancies etc. They write the trial wavefunction as an integral over a function of both real particle co-ordinates denoted R, and a set of parameters called the shadow variables, S,

$$\Psi_T(R) = \int dS \, \Xi(R, S), \tag{7.17}$$

where they take

$$\Xi(R, S) = \exp\left[- \sum_{i<j} u_r(r_{ij}) - \sum_k \phi(r_k - s_k) - \sum_{l<m} u_s(s_{lm}) \right], \tag{7.18}$$

and

$$\phi(r) = \alpha r^2 \tag{7.19}$$

with α a variational parameter, and u_r and u_s variational functions. The shadow variables are in one-to-one correspondence with the real variables and can be thought of as particles that are integrated out of the wavefunction, the shadow particles. If the u_s is chosen to be a classical potential that crystalises, this form looks like a localised form, (7.3,4) around the classical crystal positions. However, particle exchange and translational invariance are maintained since the underlying classical crystal maintains these symmetries. Of course, if the shadow variables are frozen into a particular crystalline state during a Monte Carlo simulation, there is no particular advantage to this form over the original localised form.

Two other motivations for the form (7.18, 19) were given by Vitiello et al. The first is that path integral Monte Carlo simulations can give a wavefunction of the shadow form. If we look at a Feynman path in a crystal, we see that a particle is attracted indirectly to the centre of mass of its path, and this centre of mass looks like a classical particle when interacting with the other particles' paths. The crystalisation of these paths forms the quantum crystal. The shadow co-ordinates are interpreted as these path variables. A slightly different motivation comes from the projection technique used in diffusion Monte Carlo calculations

(see Sect. 7.2) where a trial wavefunction of a pair product form, given by the shadow u_s term, is operated on by a many-body Green's function, $\exp(-\tau H)$ which is then approximated by the u_r and ϕ terms of (7.18). Since the starting function is a crystal, we expect to stay in the crystalline phase. The Green's function will build in the physical correlations between the particles, including some 3-body and higher correlations. The shadow procedure will always improve any variational trial function by building in additional correlations. A virtue of the shadow wavefunction is that the same form can be used for the liquid and solid phases and the trial function can undergo a liquid to solid transition with only a change in variational parameters just as a classical system freezes as the temperature is lowered.

The evaluation of expectation values with the shadow wavefunction is straightforward. Both the real particle and shadow particle integrations are done using the *Metropolis* et al. method. To calculate variational expectation values there are two sets of shadow variables, one for Ψ_T^* and another for Ψ_T.

A disadvantage of the shadow form is that since the shadow integration must be done to obtain $\Psi_T(R)$ from $\Xi(R,S)$, the energy variance will not be zero even for an exact trial function. This may be offset by the extra correlations built in by the projection. Of course, the shadow procedure can be systematically improved by either adding 3-body and other correlations to the shadow form, or by using a more accurate representation of the Green's function as will be discussed in Sect. 7.3.2. No work has been done along these lines. Another disadvantage of the shadow form is that the dynamics of the VMC or GFMC seem to be significantly slowed down by the entanglement of the real variables with the shadow variables so that Monte Carlo averages have more autocorrelation and converge slower. It is not clear whether one achieves lower errors per unit of computational effort by using the shadow form or by a direct GFMC calculation with a simpler trial function.

The shadow wavefunction has properties that lend it to excited state calculations in quantum fluids. The standard Feynman excitation spectrum is obtained by operating on the ground-state wavefunction with the excitation operator

$$\rho_k = \sum_j \exp(i\boldsymbol{k}\cdot\boldsymbol{r}_j). \tag{7.20}$$

In the case of shadow wavefunctions, the excitation operator can operate on the shadow variables as well as the real variables. That is the excitation operator can be taken to be

$$\sigma_k = \sum_j \exp\{i\boldsymbol{k}\cdot[\boldsymbol{s}_j + \gamma(\boldsymbol{s}_j - \boldsymbol{r}_j)]\}. \tag{7.21}$$

If it operates only on the shadow variables (i.e. $\gamma = 0$), the projection argument given above indicates that the shadow correlation will build in some state dependent effects. *Wu* et al. [7.50, 51] show that the shadow form gives backflow correlations. At the roton minimum they obtain energies within 0.5–0.8 K of experiment [7.52, 53] for a range of densities with error bars of about 0.6 K.

These calculations are difficult because of the large phase fluctuations that can occur using the excitation operator σ_k with $\gamma \neq 1$.

Another interesting result of *Wu* et al. is obtained, similarly, by applying the Feynman vortex excitation operator to the shadow variables. The vortex core no longer has a singular vorticity. The singularity is smeared out by the shadow correlations producing a much more physical vortex. Detailed numerical calculations have not yet been done.

7.1.7 Wavefunction Optimisation

With increasingly complex variational wavefunctions, better methods to determine the optimal values of variational parameters are needed. Traditionally, the expectation value of the energy is minimised to find the optimum values of the variational parameters. Although repeated calculations of the energy at various values of the variational parameters can produce good results, typically reweighting techniques are used to calculate the change in energy when optimising the parameters as described in I.

The expectation value of an operator O, with wave function ψ_{new}, can be written in terms of configurations sampled from a wavefunction ψ_{old}. These reweighting schemes often yield a much better estimate for the change in expectation value between ψ_{old} and ψ_{new} than independent calculations, since many of the fluctuations in the two calculations cancel. Often, reweighting calculations take less computer time since some parts of the calculations will be the same when using a ψ_{new} close to ψ_{old}. In any case, only independent samples from ψ_{old} are used which can further reduce the computer time required. We can write,

$$\langle O \rangle_{\text{new}} = \int dR \frac{\psi^*_{\text{new}}(R) O \psi_{\text{new}}(R)}{\psi^2_{\text{new}}(R)} w(R) P(R) / \int dR\, w(R) P(R), \tag{7.22}$$

with

$$P(R) = \frac{\psi^2_{\text{old}}(R)}{\int dR \psi^2_{\text{old}}(R)}, \tag{7.23}$$

and

$$w(R) = \frac{\psi^2_{\text{new}}(R)}{\psi^2_{\text{old}}(R)}, \tag{7.24}$$

and calculate $\langle O \rangle_{\text{new}}$ and $\langle O \rangle_{\text{old}}$ from the same set of samples of $P(R)$.

The variance of the energy is non-negative and equals zero only for the eigenstates of the Hamiltonian. Recent results on atomic and molecular electronic systems [7.15, 44, 54, 55] and on bulk ^{4}He [7.56] indicate that minimising the variance or a linear combination of the energy and variance [7.57] by reweighting methods and using standard minimisation techniques such as Levenberg–Marquardt, Simplex, or Newton's method, can optimise of the order of 10–50 parameters.

Two-body correlation factors in quantum fluids have long been optimised using integral equation methods such as the paired–phonon method of *Feenberg* and coworkers [7.58]. Recently, Monte Carlo techniques have been used to optimise correlation factors [7.56]. A simple method consists of writing the 2-body correlation as

$$f(r) = \sum_{n=1}^{N_b} a_n f_n(r), \tag{7.25}$$

where a_n are variational parameters, and $f_n(r)$ are the solutions to the 2-body Schrödinger equation

$$-\frac{1}{m}\nabla^2 f_n(r) + v(r) f_n(r) = \lambda_n f_n(r), \tag{7.26}$$

and N_b is the number of basis functions. Typical boundary conditions are those used with a single function by *Pandharipande* [7.59] such that $f_n(r)$ goes smoothly to 1 at $r = d$, with d either a variational parameter or fixed at a reasonable cutoff distance. Boundary conditions that match smoothly to the correct long-range tail at $r = d$ could be used [7.43]. This basis set has the advantage of automatically satisfying the 2-body Schrödinger equation at small r, and having reasonable behaviour at large r.

Schmidt and *Vitiello* [7.56] have used the Levenberg–Marquardt method and variance minimisation to calculate Monte Carlo optimised 2-body correlation factors in liquid and solid ^{4}He. They find energies about 0.1 K lower in both the liquid and solid than with analytic or integral equation forms. The method can be generalised to other correlations, and the basis can be refined by redefining $v(r)$ in (7.26) to be an effective two-body potential that gives a nearly optimum $f(r)$ as its f_0.

7.2 Green's Function Monte Carlo and Related Methods

7.2.1 Outline of the Method

The Green's function Monte Carlo (GFMC) method has been described in I and II, and a simple tutorial is available [7.60]. The interested reader is referred to these articles and references therein. Here we give only enough to define terms. The method simply projects a trial state to the ground state using, as a Green's function, the real space representations

$$G(R, R') = \langle R | \frac{E_T + E_C}{H + E_C} | R' \rangle \tag{7.27}$$

or

$$G(R, R', \tau) = \langle R | \exp[-(H - E_T)\tau] | R' \rangle, \tag{7.28}$$

where E_C is a constant chosen to make the spectrum of $H + E_C$ positive, and E_T is a trial energy adjusted to keep the population of Monte Carlo walkers constant and equals the ground state energy. The Schrödinger equation becomes,

$$\Psi(R, \tau + \Delta\tau) = \int dR' G(R, R', \Delta\tau)\Psi(R', \tau), \tag{7.29}$$

and

$$\Psi(R, n+1) = \int dR' G(R, R')\Psi(R', n), \tag{7.30}$$

for (7.28) and (7.27) respectively, which both converge to the ground state of the Hamiltonian. Since the version using $G(R, R', \tau)$ maps the Schrödinger equation in imaginary time onto a diffusion equation, it is often referred to as diffusion Monte Carlo (DMC).

In II, both exact and short time versions of the diffusion Monte Carlo method were discussed. Versions with higher order accuracy in the time step than the simple short time approximation, have also been developed [7.61].

7.2.2 Fermion Methods

While giving good results for Bose ground-states, both methods suffer from exponentially growing variance when naively applied to fermion problems. If the negative signs associated with the antisymmetric wave function are carried along as weights, the method is known as transient estimation. A common technique, the fixed-node approximation, is to solve (7.29) or (7.30) in the region where a fermi trial function is positive. See II for a review of some GFMC methods for fermions. Some progress has been made in formulating fermion algorithms. Straightforward improvements of the fixed-node approximation can be made by regulating the walkers that cross the nodes, or by introducing softer boundary conditions at the nodes. The method of mirror potentials has been developed by *Kalos* and *Carlson* [7.62]. This method attempts to improve on the fixed-node approximation by writing the antisymmetric ground-state wave-function as

$$\Psi^A = \Psi^+ - \Psi^-, \tag{7.31}$$

where Ψ^+ and Ψ^- are positive functions and the Schrödinger equation can be trivially rewritten as two coupled equations,

$$[H + c(R)\Psi^+]\Psi^- = E\Psi^-, \tag{7.32}$$

and

$$[H + c(R)\Psi^-]\Psi^+ = E\Psi^+. \tag{7.33}$$

The original Schrödinger equation is recovered by subtraction, and the function $c(R)$ can be chosen arbitrarily. The mirror potential is the additional $c(R)\Psi^{\pm}$ in the coupled equations, and is defined by the population of the oppositely signed walkers. Unfortunately, these walker populations are not normally dense enough in real simulations to make well defined mirror potentials, and

approximate trial functions are used instead. The method then loses some of its appeal. By varying the magnitude of the function $c(R)$ in (7.32) and (7.33). the approximate mirror potential method can be made to interpolate between fixed node and transient estimation results.

Calculations for lattice fermion systems, have been made using the *Stratonovich-Hubbard* transformation [7.63, 64]. The pairwise interaction is replaced by auxiliary fields. The fermion part of the wavefunction can then be solved, since the fermions will then only interact via the auxiliary fields. These fields are averaged using the Monte Carlo method. Some attempts at formulating this technique for continuum systems have been made, for example, by *Sugiyama* and *Koonin* [7.65], and a constraint similar in spirit to the fixed-node approximation has been implemented by *Fahy* and *Hamann* [7.66]. However, much more work needs to be done before these methods can be applied to quantum liquids, where the number and magnitude of the auxiliary fields is large due to the continuous nature of the motion of the particles, and the range and strength of the interactions. It is difficult to use the insight provided by the pair-product and backflow trial functions to reduce the computational time once auxiliary fields have replaced the pair interaction.

7.2.3 Shadow Importance Functions

In both Green's function Monte Carlo and diffusion Monte Carlo, importance sampling is introduced to lower the variance in the Monte Carlo walk. As discussed in I, this is simply accomplished by replacing the iterative equation, (7.29) by

$$\Psi(R, n+1)\Psi_T(R) = \int dR' \frac{\Psi_T(R)}{\Psi_T(R')} G(R, R')\Psi(R', n)\Psi_T(R'), \tag{7.34}$$

and solving for $\Psi_T(R)\Psi(R, n)$, using the importance sampled Green's function

$$\frac{\Psi_T(R)}{\Psi_T(R')} G(R, R'). \tag{7.35}$$

The use of a shadow wavefunction $\Psi_T(R) = \int dS \Xi(R, S)$ as the importance function introduces some extra difficulty, since the integral over the shadow variables must be done by Monte Carlo. *Vitiello* et al. [7.67, 68] show that one method to accomplish this consists of making an arbitrary number M_r of GFMC steps with an importance function given by $\Xi(R, S)$ with fixed S, followed by an arbitrary number of *Metropolis* et al. steps M_s on the shadow variables S, at the fixed values of the real variables, satisfying the usual detailed balance condition,

$$\Xi(R, S')P(R, S' \to S) = \Xi(R, S)P(R, S \to S'), \tag{7.36}$$

where $P(R, S \to S')$ is the Metropolis transition probability for the shadow variables at fixed value of the real variables. The average results are independent

of the values of M_r and M_s, but the variance and autocorrelations, of course, will depend on these choices. Vitiello et al. report good results with $M_r = M_s = 1$ although the use of the shadow trial function increases the computation time needed for convergence by about one order of magnitude. Other methods of sampling the shadow variables such as direct incorporation into the GFMC sampling, Langevin, or molecular dynamics methods could also be used.

7.3 Path Integral Monte Carlo Method

Path integral Monte Carlo (PIMC) has emerged in the last few years as an extremely powerful computational method for computing properties of quantum fluids and solids at non-zero temperature, complementing the GFMC methods used at zero temperature. There has been an enormous amount of work using finite temperature methods on lattice models for applications in lattice gauge theory and high temperature superconductivity which is covered elsewhere in this volume.

7.3.1 PIMC Methodology

All static properties and some dynamical properties of a quantum system in thermal equilibrium are obtainable from the density matrix

$$\rho(R, R'; \beta) = \sum_\alpha e^{-\beta E_\alpha} \phi_\alpha^*(R) \phi_\alpha(R'), \tag{7.37}$$

a sum over the exact energy eigenstates of the Hamiltonian weighted by the Boltzmann factor. As seen by direct substitution, the density matrix satisfies the convolution identity

$$\begin{aligned} \rho(R, R', \beta) = \int \cdots \int dR_1 dR_2 dR_3 \cdots dR_{M-1} \rho(R, R_1, \tau) \\ \cdot \rho(R_1, R_2, \tau) \cdots \rho(R_{M-1}, R', \tau), \end{aligned} \tag{7.38}$$

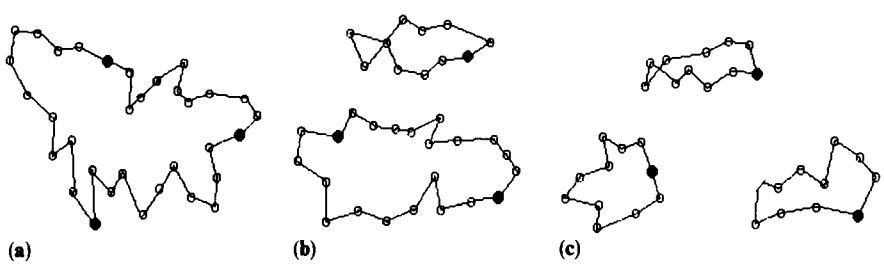

Fig. 7.1 a–c. Three types of exchange possible among three atoms. The circles represent the co-ordinates of the atoms at a given time slice with the filled circles denoting the first time slice. The lines represent the "spring" or kinetic energy part of the action and connect the same atom on neighbouring time slices

where $\tau = \beta/M$. As M is increased and τ approaches zero (the high temperature limit), one can write down an explicit approximation to the density matrix. The simplest, but by no means the recommended form, is the semiclassical or primitive form

$$\rho(R, R', \tau) = (4\pi\lambda\tau)^{-3N/2} \exp\left[-\frac{(R-R')^2}{4\lambda\tau} - \tau V(R) \right], \tag{7.39}$$

where $\lambda = \hbar^2/2m$. Substituting this approximation into the convolution identity yields the Trotter formula. A quantum observable can be obtained by averaging over the probability density: e^{-S} where the "action" is defined as

$$S = \sum_{i=1}^{M} \frac{(R_i - R_{i-1})^2}{4\lambda\tau} + \tau V(R_i), \tag{7.40}$$

for sufficiently large M. The $3N$-dimensional points R_i for $0 \leqq i \leqq M$ define the path which is periodic in the index i, that is $R_0 = R_M$. This probability distribution is similar to the classical Boltzmann distribution of a system of ring "polymers" having a harmonic spring interaction between neighbouring beads on the same polymer and with beads on different polymers interacting via the original potential function $V(r)$ as shown in Fig. 7.1a. Classical simulation techniques can be used to perform the $3NM$-dimensional path integral but one must be careful to ensure that the simulation will converge in a reasonable amount of computer time as we will discuss below.

Bose statistics introduce a very profound, yet simple, change in these paths. One can obtain the boson density matrix [7.69] from the unsymmetrised density matrix by applying a symmetrisation operator,

$$\rho(R, R', \tau) = \frac{1}{N!} \sum_{P} \rho(R, PR', \tau). \tag{7.41}$$

The sum is over the permutations P of the particle labels. This simply means that the polymers are allowed to reconnect in any manner they like, as seen in Fig. 7.1b,c for 3 atoms. For Bose systems, the Monte Carlo procedure must average both over ways of connecting the polymers and the paths for a given connection. Superfluidity is simply the formation of a "macromolecule" which stretches across the system.

There are two very important considerations in actually carrying out the simulation. First, the approximate high temperature form for the density matrix should be made as accurate as possible to reduce the value of M and, second, the dynamics of the simulation must be chosen carefully in order to have an algorithm which is effectively ergodic in permutation and path space.

7.3.2 The High Temperature Density Matrix

Although the primitive form for the action gives the right limit as the time-step goes to zero, its use in simulations is inefficient. Luckily, it is relatively easy to

find a more accurate expression for the high temperature density matrix. For a soft potential, e.g. the harmonic oscillator or a lattice model, one can use an improved action derived from an $\hbar$, Wigner–Kirkwood (WK) [7.70] expansion

$$\delta S = \frac{\lambda}{12}\sum_{i,k}(\tau^2 F_{ik}^2 + 2\tau\nabla F_{ik}) + O(\lambda^2), \tag{7.42}$$

where F_{ik} is the classical force on the ith particle in "time-slice" k. Such an expansion is not appropriate for helium because the major corrections to the density matrix come from small r. For a potential like r^{-12} the WK corrections will be order r^{-26} but quantum diffraction effects tend to smooth the potential to r^{-5}. One needs an expansion appropriate to a hard sphere-like system.

One can generalise the Feynman–Kacs formula for the density matrix [7.71] to get an exact non-perturbative correction to any density matrix $\rho^{(n)}$,

$$\rho(R,R',\tau) = \rho^{(n)}(R,R',\tau)\left\langle \exp\left\{ -\int_0^\tau dt E_n[R(t),R';\tau-t]\right\}\right\rangle_{\text{DRW}}, \tag{7.43}$$

where DRW denotes an average over all drifting random walks from R to R', and E_n is the "local energy" of $\rho^{(n)}$,

$$E_n(R,R';\tau) = \frac{1}{\rho^{(n)}(R,R',\tau)}\left(H + \frac{d}{d\tau}\right)\rho^{(n)}(R,R',\tau). \tag{7.44}$$

Starting with the free particle density matrix, and approximating the average by assuming that pairs of atoms diffuse independently of the other atoms, one arrives at the pair-product form [7.72] for the high temperature density matrix,

$$\rho^{(1)}(R,R',\tau) = \rho^{(0)}(R,R',\tau)\exp\left[-\sum_{i<j} u(r_{ij},r'_{ij};\tau)\right], \tag{7.45}$$

where $\rho^{(0)}$ is the free particle density matrix and u is defined to be exact for exactly two atoms. This will go over to the Jastrow wavefunction at zero temperature. To use this density matrix, one must make a numerical estimation of the exact two-atom density matrix at high temperature. It is convenient to transform the two-atom Bloch equation into spherical relative coordinates and then to solve for the radial density matrices using the matrix squaring method [7.73]. As an alternative, for hard sphere or coulomb potentials, one can use their eigenfunction expansions. The pair density matrices are functions of three co-ordinates. It is convenient [7.74] to use the variables $q = (1/2)(|r_{ij}| + |r'_{ij}|)$, $s = |r_{ij} - r'_{ij}|$ and $z = |r_{ij}| - |r'_{ij}|$. Since s and z will be order of $\sqrt{\tau}$ one can expand u as

$$u(r_{ij},r'_{ij};\tau) = \sum_{n,l} u_{nl}(q)s^{2n}z^{2l}. \tag{7.46}$$

Ceperley and *Pollock* [7.75] have found that if the exact two-atom density matrix is used in liquid ^{4}He, τ can be chosen as large as $0.025\,\text{K}^{-1}$, and one can still obtain total energies accurate to 0.1 K. Thus at least 20 time slices are needed for a simulation for superfluid ^{4}He.

In case even higher accuracy is needed, one can go to the next order by finding the local energy of $\rho^{(1)}$, and then make a trapezoidal approximation

$$\rho^{(2)}(R, R', \tau) = \rho^{(1)}(R, R', \tau) \exp\left[\frac{\lambda\tau}{3}\sum_i (\nabla_i U)^2\right], \tag{7.47}$$

where $U = \sum_{i<j} u(r_{ij})$ is the 2-body action. This density matrix, $\rho^{(2)}$, has the same functional form as the 3-body trial function discussed in Sect. 7.1.3.

7.3.3 Monte Carlo Algorithm

The numerical evaluations of the path integrals for many-body systems have been performed with either the classical Molecular Dynamics or Metropolis Monte Carlo methods. The Molecular Dynamics technique is straightforward to apply, but does not allow the possibility of making a permutational move so we will not discuss it further. Let us briefly recall the Metropolis rejection method. A Markov chain is generated based on some a priori transition probability, $T(R'|R)$, which is the probability density of sampling the trial move R' based on the old point R. Then that move is accepted with probability

$$A(R'/R) = \min\left[1, \frac{T(R|R')e^{-S(R')}}{T(R'|R)e^{-S(R)}}\right], \tag{7.48}$$

where $S(R')$ and $S(R)$ are the actions in the old and new state. In a Metropolis method it is possible to mix up moves in any blend as long as the probability of making a given type of move is independent of the system state, and each type of move individually satisfies the detailed balance relation. Eventual convergence is guaranteed by the detailed balance condition but the rate of convergence can be very slow, particularly with path integrals. A common theme in all the improved methods is that the slow convergence is a consequence of the kinetic energy term of the action in the limit of small τ. But it easy to device a way to sample this term a priori. Below we list the various types of Metropolis transitions that have been proposed. Unfortunately there is little comparison of their efficiencies in the literature.

7.3.4 Simple Metropolis Monte Carlo Method

In the simplest choice for the transition probability, a single atom at a single time slice, a "bead", is displaced uniformly inside a cube of side Δ, with Δ adjusted to achieve 50% acceptance. As M increases the random walk diffuses through configuration space very slowly because the largest displacement allowed by the free particle density matrix is order $\sqrt{(\lambda\tau)}$. Even worse, an atomic path acquires an inertia, so that in following moves, fluctuations away from the centre of mass are suppressed. As a consequence, it is difficult to achieve convergence in a reasonable number of steps.

7.3.5 Normal Mode Methods

The kinetic energy term for each atom can be diagonalised by working with the fourier coefficients,

$$Q_k = \sum_{l=1}^{M} R_l e^{-\pi i k l/M}. \tag{7.49}$$

The kinetic part of the action then has an expansion

$$S = \frac{1}{\lambda\beta}\sum_k \sin^2\left(\frac{\pi k}{m}\right)|Q_k|^2, \tag{7.50}$$

and each of the $3NM$ variables, Q_k, can be sampled independently from the resulting Gaussian distribution. In the absence of a pair potential, all moves would be accepted. When a realistic potential is present the large k modes can be sampled directly from the above distribution since they cause only a small movement of the path. Usually the long wavelength modes are moved a small amount, say $|Q_k' - Q_k| < \gamma_k$, with γ_k adjusted to get 50% acceptances. The centre of mass mode ($k = 0$) is treated separately and moved as a classical particle [7.76–78].

7.3.6 Threading Algorithm

In this method, one cuts out a section of one or several atomic positions for n time slices. Then one recursively generates a new path by growing from time slice 0 to slice n with the diffusion algorithm

$$R_{i+1} = R_i - 2\tau\lambda\nabla S_T[R_i, R_n; (n-1)\tau] + \eta_i\sqrt{(2\tau\lambda)}, \tag{7.51}$$

where η_i is a normally distributed random vector with zero mean and unit variance and S_T is a trial action. Note that the time argument of S_T will be greater than τ if more than one time-slice is being updated. The trial action is only used to guide the walk and any convenient approximation can be used for it. Inaccuracies will only affect the acceptance ratio, not the converged distribution. After the new path is generated, it is accepted or rejected in the usual Metropolis fashion based on the difference between the old and new action and on the ratio of the sampling probabilities for the old and new paths. The advantage of this method over the previously discussed ones is that a completely new path can be generated and several atoms can be simultaneously updated. The form of the diffusion can be shown to be optimal in the sense that if the trial action were exact with all atoms being moved and τ were sufficiently small, the acceptance ratio would be one. However, in practice, moves of more than a few time slices are often rejected [7.71].

7.3.7 Bisection and Staging Methods

The bisection method is closely related to the Levy method of constructing a Brownian bridge. To construct a random walk from $R(0)$ to $R(\beta)$ in time β,

one begins by sampling the trajectory at the midpoint as

$$R(\beta/2) = \tfrac{1}{2}(R(0) + R(\beta)) + w_\beta \eta, \tag{7.52}$$

where η is a normally distributed random vector of zero mean and unit variance and $w_\beta = \sqrt{\lambda\beta/2}$. One then bisects the time intervals $(0, \beta/2), (\beta/2, \beta)$ to find the points $R(\beta/4)$, $R(3\beta/4)$ etc. until one has sampled all the points on the path.

In the bisection method [7.74], a move consists of several levels; the first level is the midpoint, the next level consists of the two midpoints of the midpoint etc. A decision is made at the end of each level whether to continue on to the next level or to reject the entire attempted move. Only when one reaches the final level are the co-ordinates updated. There are two ingredients in this algorithm. The first is the method of sampling the midpoints. It has been found best to use a correlated Gaussian distribution so that the midpoint is sampled according to

$$R(\beta/2) = \tfrac{1}{2}(R(0) + R(\beta)) - w_\beta^2 \nabla U + \eta, \tag{7.53}$$

where U is the interaction part of the action and η is sampled from a normally distributed random number with zero mean and covariance

$$\langle \eta\eta \rangle = w_\beta^2 (I - w_\beta^2 \nabla\nabla U). \tag{7.54}$$

This correlated normal distribution is sampled using a Choleski decomposition of the covariance matrix. The effect of atomic interactions on the a priori distribution is to push the mean position of an atom away from its free particle mean if another atom is there. This is similar to the techniques of "force-bias" Monte Carlo and "smart Monte Carlo" [7.45]. The covariance has a crucial role to play when an exchange of atoms is being attempted in order to change the permutation. Then the covariance keeps the two (or more) moving atoms out of each other's way.

The second ingredient is the rule for accepting a given level and proceeding onto the next level. For simplicity, let us consider only the acceptance of the midpoint move $R'_{n/2}$ which has been sampled from the correlated Gaussian distribution $T(R'_{n/2})$. The probability to go onto the second level is given by

$$\min\left[1, \frac{T(R_{n/2})\pi_2(R'_{n/2})}{T(R'_{n/2})\pi_2(R_{n/2})}\right], \tag{7.55}$$

where

$$\pi_2(R_{n/2}) = \frac{\rho(R_0, R_{n/2}; n\tau/2)\rho(R_{n/2}, R_n; n\tau/2)}{\rho(R_0, R_n; n\tau)}. \tag{7.56}$$

Note that one must compute the probability of sampling the old midpoint and the old action.

For multi-level sampling, until the final level, the density matrices will have time arguments greater than τ. The approximation made will only affect the rate of convergence, not the final converged values of physical quantities. But as the density matrices approach the exact ones, and the sampling $T(R_i)$ approaches its optimal value, the acceptance ratio approaches unity. In the bisection algorithm, the parameter which controls the size of the move is the number of time steps. The advantage of the bisection method over the threading method is that places of high potential energy are most likely at the midpoint. Unfavourable moves can be quickly identified and the process stopped instead of continuing on to the inevitable rejection.

The staging algorithm, which has been applied to a single electron in a classical liquid [7.79], has ideas similar to the bisection method. The first level is constructed using with the Levy algorithm and then a second level repeatedly sampled to find the action of the first level. This is not as efficient as the bisection procedure because the amount of computation per accepted move is much higher.

7.3.8 Sampling Permutations

The simplest Monte Carlo algorithm to change the permutation for a Bose system, would involve interchanging a pair of particle labels without moving the chain at all. This will not sample permutation space for small τ as the following argument demonstrates. In relative co-ordinates, a pair of ^{4}He atoms will move on the average $\sqrt{\lambda\tau} = 1$ A for a time step of 1/40 K. As can be seen in Fig. 7.2, since the relative co-ordinates are about 3 A apart because of the pair potential, there is a very small chance (about $10^{-5} = \exp[-\sigma^2/(4\lambda\tau)]$) of making an exchange. In order to fully explore the configuration space of a superfluid, it is necessary to couple permutation moves with moves of a portion of the polymer chains of the atoms being relabeled.

It can be shown that the optimal function to sample a permutation P from is $\rho(R_i, PR_{n+i}; n\tau)$. To have a reasonable acceptance probability one wants the move to be as small as possible. Let us suppose that the permutation change, P, ranges over all cyclic permutations involving 2, 3 or 4 atoms. It is important to go beyond pair interchanges in a dense liquid since it is easier for three of

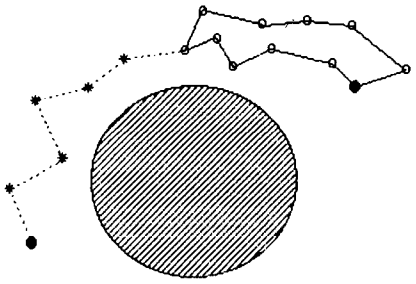

Fig. 7.2. Direct (solid) and exchange paths (dashed) for two atoms in relative co-ordinates. The shaded circle indicates the portion of phase space excluded by the interatomic potential. In relative co-ordinates an exchange path proceeds from a point Δ to a point $-\Delta$ while a direct path is a loop. The figure shows that a substantial change in the path variables are needed to move from a closed loop to an exchange path

four atoms to cyclically permute than it is for a pair. Since the exact density matrix is unknown, some approximation must be made to construct the a priori chance of a permutation. The free particle density matrix is a convenient choice. Then the probability of attempting a permutation P is proportional to

$$T(P) = \exp\left[-\frac{(R_i - PR_{n+i})^2}{4n\lambda\tau} \right]. \tag{7.57}$$

A table of these probabilities can be quickly constructed and sampled since it only involves inter-atomic distances between time slice i and slice $i+n$. If the total permutation and path are accepted, the table needs to be updated.

7.3.9 Calculation of the Energy

The most straightforward way to calculate the energy is to differentiate the partition function with respect to the temperature;

$$E = -\frac{d\ln(Z)}{d\beta} = \frac{3N}{2}\tau + \frac{1}{M}\sum_{i=1}^{M}\left\langle -\frac{(R_i - R_{i-1})}{4\lambda\tau^2} + \frac{dU_{i,i-1}}{d\tau} \right\rangle, \tag{7.58}$$

where the brackets indicate average over the walk and $U_{i,i-1}$ is the interacting part of the action as defined in (7.45) between time slices i and $i-1$. At sufficiently small τ, this reduces to the potential energy but (7.58) is exact at any τ for an exact expression for the action. In taking the β derivative, the order of an approximation to the action will be reduced by one, so if the expression for the action has an error of order τ^3, this expression for the energy is only correct to order τ^2. For that reason, it is best to include the force squared term of (7.47). If U is the solution to the two-body problem, its time derivative can be eliminated in favor of spatial derivatives. A comparison of the two will give an estimate of the systematic error of the energy [7.76].

There is a difficulty in using (7.58) to estimate the energy, namely its error grows as τ^{-1}. Thus attempts have been made to find lower variance estimators [7.71, 80, 81]. It is possible to eliminate the troublesome kinetic energy term by integrating by parts over the path variables, and using a form reminiscent of the virial expression for the pressure;

$$E = \frac{3N}{2\beta} + \frac{1}{M}\sum_{i=1}^{M}\left\langle \frac{dU_{i,i-1}}{d\tau} - \frac{F_i\Delta_i}{2} - \frac{1}{4\beta\tau\lambda}(R_{M+i} - R_i)(R_{i+1} - R_i) \right\rangle, \tag{7.59}$$

where F_i is the analog of the classical force

$$F_i = -\frac{1}{\tau}\nabla_i(U_{i,i-1} + U_{i,i+1}), \tag{7.60}$$

and Δ_i is the deviation from the particle's centroid

$$\Delta_i = \frac{1}{2M}\sum_{j=M+1}^{M-1}(R_i - R_{i+j}). \tag{7.61}$$

This virial estimator is exact (if the exact U is used) but care must be taken in interpreting terms $(R_i - R_j)$ to ensure the atoms have always continuous trajectories with periodic boundary conditions and bosonic exchange. For free particles, we can obtain the following estimator for the energy,

$$E = \frac{3N}{2\beta} - \left\langle \frac{(R_0 - R_M)^2}{4\beta^2\lambda} \right\rangle, \tag{7.62}$$

where the difference in distances may include winding around the periodic boundaries of the box and bosonic exchange. Quantum free particles in a box can have an energy less than $\frac{3}{2}kT$; witness bose condensation. Only the primitive estimator has been applied for superfluid helium since the virial does not have lower variance for the τ and potentials used.

7.3.10 Computation of the Superfluid Density

The path integral framework translates superfluidity into very intuitive concepts. As is discussed in Feynman's papers, at approximately 2 K the polymers become long enough so that exchange becomes probable. The partition function will increase as this new phase space opens up and the second derivative of it, the specific heat, will have the familiar lambda shape. Figure 7.3 shows the probability of a given atom participating in a cyclic exchange of n atoms, as calculated with PIMC.

Superfluidity is experimentally defined by the equilibrium response of the system to a gentle motion of the walls. If the walls are rotated slowly, the normal fraction will be entrained with the walls at equilibrium while the superfluid will remain at rest. By doing a transformation from a co-ordinate frame where the walls are moving to one where they are at rest, it is possible to use PIMC to determine the dependence of the free energy on the motion of the walls. The superfluid density is proportional to the second derivative of the free energy with respect to the wall velocity at zero velocity, and in periodic boundary conditions can be shown [7.82] to be equal to the mean squared number of paths in PIMC which wind around the periodic walls,

$$\frac{\rho_S}{\rho} = \frac{\langle W^2 \rangle}{2d\lambda\beta N}, \tag{7.63}$$

where **W** is the winding number,

$$\boldsymbol{W} = \sum_i \int_0^\beta dt \frac{\boldsymbol{dr}_i}{dt}. \tag{7.64}$$

The winding number which describes the net number of times the paths have wound around the periodic cell is an invariant of the path. For a system without boundaries such as a droplet, one can define the normal fluid mass as that part of the system which contributes to the moment of inertia.

$$\frac{\rho_s}{\rho} = 1 - \frac{I}{I_c} = \frac{2\langle A^2 \rangle}{I_c\lambda\beta}, \tag{7.65}$$

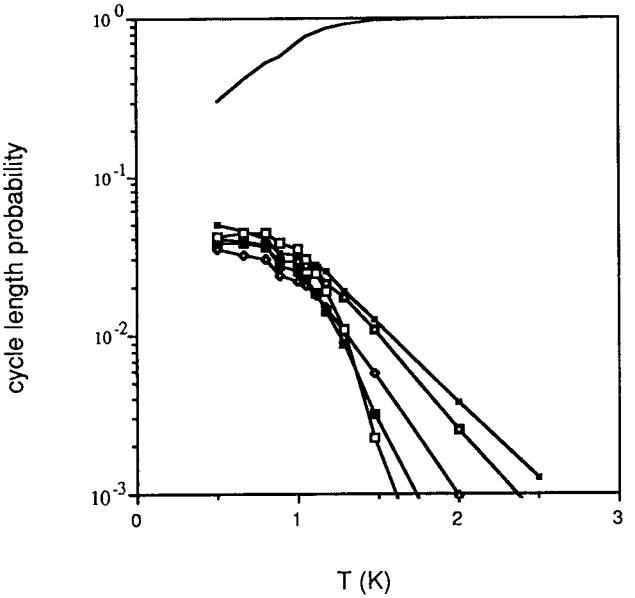

Fig. 7.3. The probability of a given atom being involved in an exchange in 2D ^{4}He as a function of temperature. The upper curve are non-exchanging atoms while the 5 lower curves are the probabilities of exchange with 2–6 other atoms. Because there are a total of 25 atoms in the simulation these probabilities approach 1/25 at low temperature. The Kosterlitz–Thouless superfluid transition occurs at a temperature of 0.7 K

where $I_c = \left\langle \sum_i r_i^2 \right\rangle$ and A is the area swept out by the paths,

$$A = \frac{1}{2} \sum_i \int_0^\beta \frac{d\boldsymbol{r}_i}{dt} \times \boldsymbol{r}_i. \tag{7.66}$$

An example of winding is shown in Fig. 7.4 and the results for the superfluid density are given in Sect. 7.4. A major difficulty in the PIMC calculations is getting the winding numbers to converge, since a change in winding number can only occur with a global change in path configuration. It has been shown recently that an estimator [7.83] based on the local diffusion of paths can give an alternative method of calculating superfluid density.

7.3.11 Exchange in Quantum Crystals

Crystal ^{3}He at millikelvin temperatures is one of the simplest and cleanest examples in nature of a lattice-spin system. Its magnetic properties result from infrequent atomic exchange, since it is only through exchange that the Pauli exclusion principle comes into play. Careful analysis of experimental data made plausible the model that the frequency of exchange of two, three, and four atoms

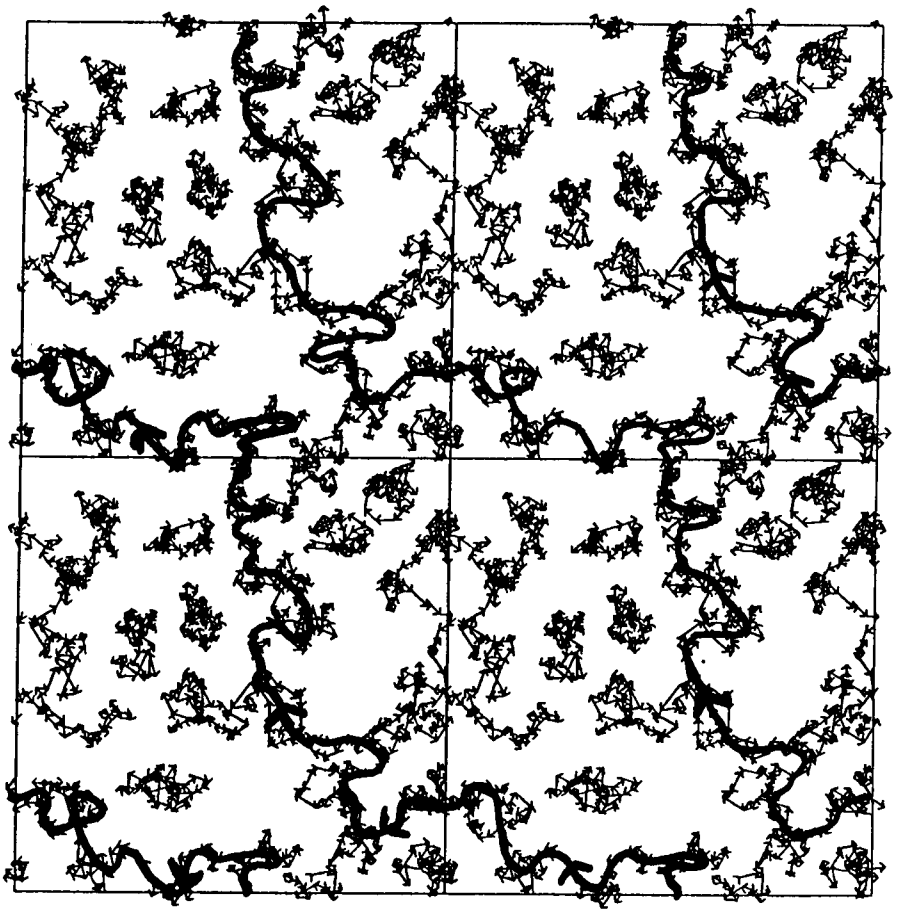

Fig. 7.4. A typical path configuration at $T = 0.8\,\mathrm{K}$ in 2D liquid ^{4}He. The basic periodic cell is replicated 4 times. There are a total of 25 atoms present. The heavy line indicates a path winding across the cell in both the x and y directions

are approximately equal to each other, but calculation of exchange frequencies is necessary for the model to be verified [7.84, 85].

To define the exchange frequencies and the lattice-spin model, one assumes that most of the time the atoms are close to lattice sites. The $N!$ degeneracy of arranging N atoms onto N lattice sites is broken by the exchanges. Suppose we allow only two ways of arranging the atoms which we will denote as Z and PZ. Here P is a permutation and Z the perfect lattice vector of $3N$ positions. Then the ground state is split into an even and odd state and the frequency with which the system oscillates between the two localised states is $2J_P = E_1 - E_0$. At low temperatures, the system of spin 1/2 fermions is described by a lattice Hamiltonian acting only on the spins: $\sum_P J_P(-1)^P P_\sigma$.

The exchange frequencies are difficult to calculate since the helium atoms have large zero point motion and correlation. Variational methods fail since they require knowledge of the wavefunction in regions where it is very small. For temperatures well below the Debye temperature only the two lowest states will contribute to the density matrix, and if we consider the element of the density matrix connecting Z with PZ it can be shown that

$$\tanh[J_P(\beta - \beta_P)] = \frac{\rho(Z, PZ; \beta)}{\rho(Z, Z; \beta)}. \tag{7.67}$$

Expanding the density matrices in terms of path integrals as in (7.38) and speaking in terms of the polymer picture, the quantum exchange rate is related to the free energy necessary to "cross-link" two or more "polymers" in a "polymer crystal". It is then possible to take the computer method developed to simulate superfluid ^{4}He and thereby find these magnetic coupling constants in the crystal ^{3}He. The results are in quite good agreement with experiment and show that many exchanges are relevant in a quantum crystal and that a quantum crystal is more complex than previously thought.

This calculation is technically demanding. Bennett's method [7.86] of the two sided acceptance ratio was used to determine the free energy ratio. To calculate the above ratio we define the state of the walk to consist not only of the path, but also of the connection of the endpoints which is either P or I (the identity permutation). Just as for superfluids, the Monte Carlo moves must allow for transitions between these two states. It is actually not necessary to make moves between the two states but only necessary to compute the acceptance probabilities for proposed transitions. Then the exchange rate is not expressed as the difference between two eigenvalues but as the ratio of two rates. The error is independent of the magnitude of the exchange frequency which is on the order of 460 μK in ^{3}He and 4 μK in ^{4}He. It is quite important in this calculation to have an accurate high temperature density matrix.

7.3.12 Comparison of GFMC with PIMC

GFMC and PIMC are very closely related methods since both are based on sampling of the thermal density matrix. The density matrix is a solution of the Bloch equation

$$-\frac{d\rho(R, R', \beta)}{d\beta} = H\rho(R, R', \beta), \tag{7.68}$$

which is the "dynamics" of the GFMC algorithm. The object held in the computer's memory in GFMC is an ensemble of configuration walkers $\{R\}$ while in PIMC it is the entire imaginary time path R_i and the permutation. The dynamics in GFMC is that of a branching random walk with an assumed guiding function while in PIMC it is a generalised Metropolis method. Insight into the physics may influence the transition probability in PIMC. GFMC can

calculate energies very accurately but has difficulty with other quantities. Estimates coming from PIMC have larger statistical errors, but they have less systematic error since they do not have the bias from the importance function. GFMC usually converges faster since the walks are less constrained while PIMC has a kind of critical slowing down as the time step goes to zero. But of course, one is comparing apples and oranges since GFMC is the method of choice for calculation of ground state properties and PIMC for calculations at non-zero temperatures.

7.3.13 Applications

There have been numerous applications [7.87] of PIMC to the situation where a single quantum particle (for example an electron or muon) is inserted into a classical system. Examples are an electron in gaseous classical helium, or a single electron on a protein. Without the possibility of particle exchange, getting the system to converge is not difficult, but on the other hand, to reach room temperature takes on the order of one thousand electron steps, much more than is needed for liquid helium because an electron is so much lighter than a He atom. There have also been PIMC calculations on almost classical systems like liquid argon, neon, and water. Monte Carlo methods used on those systems are straight-forward generalisations of the classical Monte Carlo or molecular dynamics methods, since quantum exchange is not taken into account. The results of the PIMC method that we will discuss in Sects. 7.4–6 are the applications to systems of liquid and solid helium.

7.4 Some Results for Bulk Helium

7.4.1 ^{4}He Results

The bulk ^{4}He liquid and solid ground-state behaviour is well characterised by the variational wavefunctions described in Sect. 7.1, and good equation of state results are obtained using the GFMC method. In Fig. 7.5, we show the equation of state of liquid ^{4}He at zero temperature from experiment [7.36], GFMC [7.88], and variational wavefunctions with 2- and 3-body correlations [7.89]. Figure 7.6 shows similar results for solid ^{4}He where there are small discrepancies between experiment [7.90] and the GFMC calculation which may be due to 3-body potential energy contributions. The variational results in the liquid and solid are qualitatively correct and in reasonable quantitative agreement. Figure 7.7 shows the GFMC and experimental [7.91] 2-body distribution function $g(r)$. The agreement between experiment and theory is quite good.

Simple shadow wave functions, (7.18), reduce the variational energy at the equilibrium liquid density of ^{4}He by about 0.31 K from a pure Jastrow trial wavefunction. This can be compared with about 0.85 K reduction for a 2- and

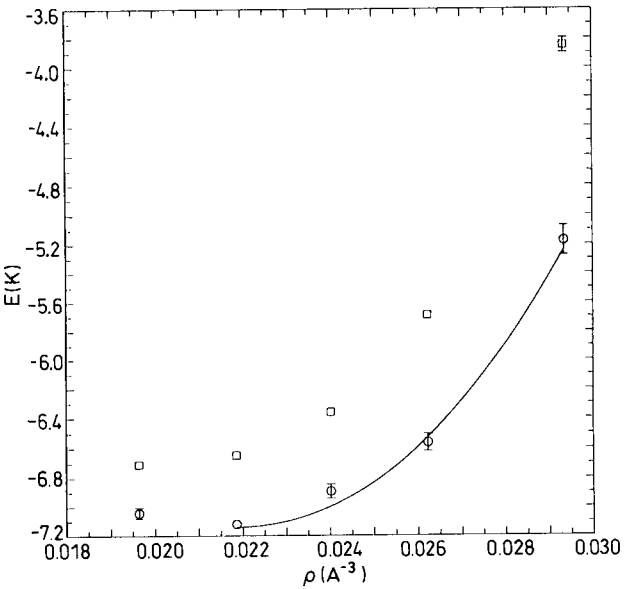

Fig. 7.5. The ground-state energy of liquid ^{4}He as a function of density. The solid line is experiment [7.36], the circles are the GFMC results [7.88], and the squares are variational results for a simple McMillan Jastrow factor and a three-body term as in (7.5–7). Points without error bars have statistical errors less than the symbol size

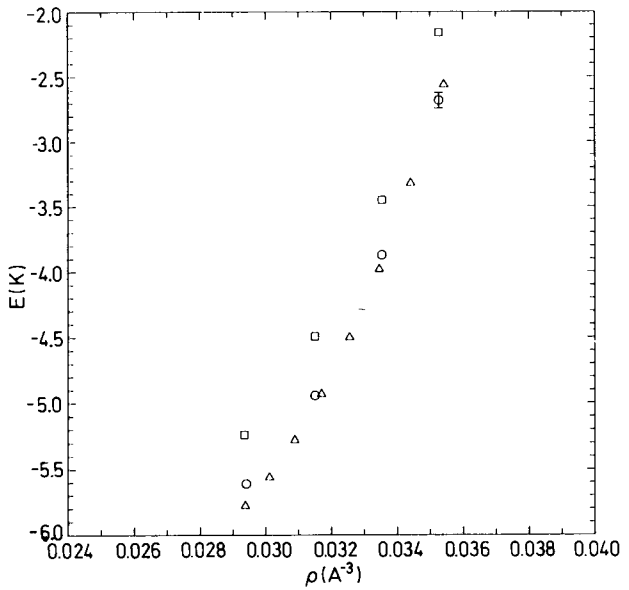

Fig. 7.6. The ground-state energy of solid ^{4}He as a function of density. The notation is the same as Fig. 7.5, except that triangles are the experimental results for the hexagonal close packed crystal [7.90]. The variational and GFMC results are for a face centred cubic crystal, and use a one-body localisation factor, (7.4), around the lattice sites

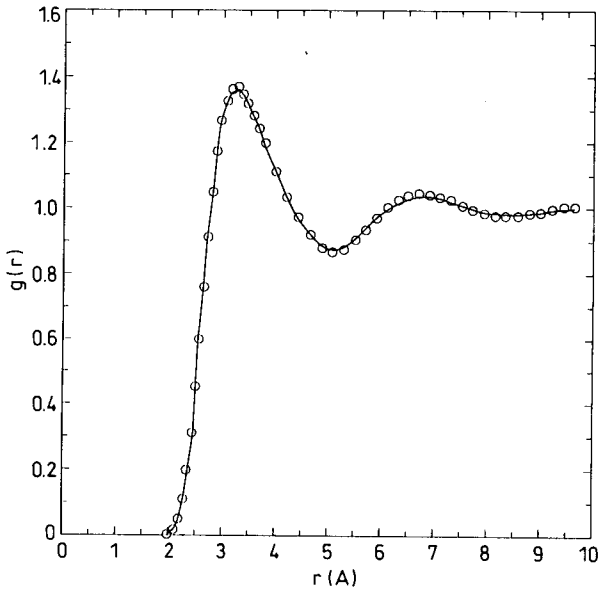

Fig. 7.7. The experimental (at 1.0 K) [7.91] (circles) and GFMC [7.88] extrapolated (solid line) two-body distribution functions $g(r)$ for liquid ^{4}He at equilibrium density

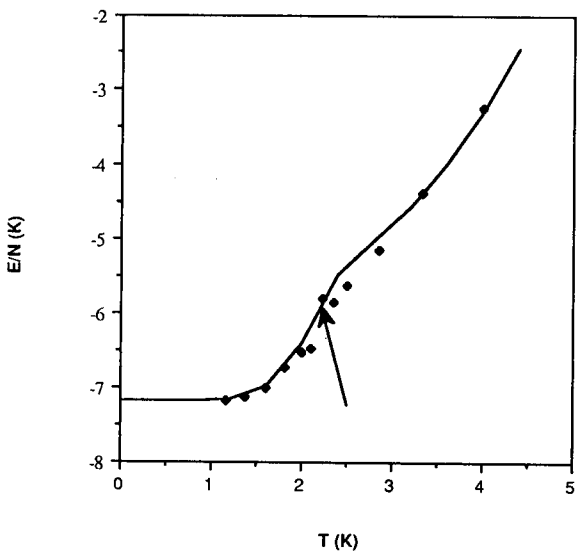

Fig. 7.8. The energy per atom of liquid ^{4}He as a function of temperature at SVP conditions as computed with PIMC (points) and measured (the curve). The arrow indicates the experimental superfluid transition temperature

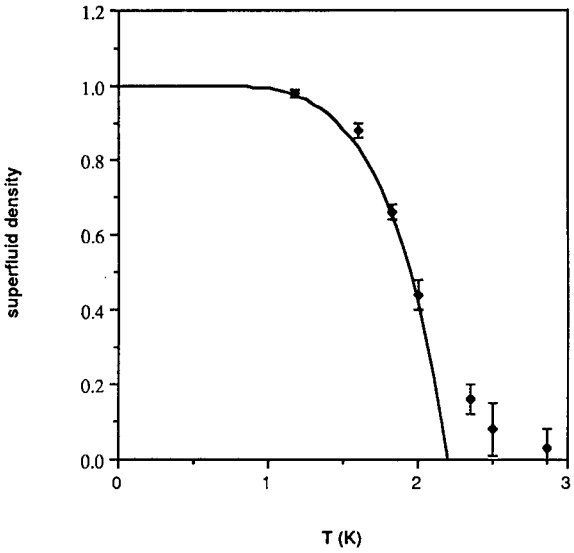

Fig. 7.9. The super-fluid density as a function of temperature at SVP conditions as computed with PIMC (points) and measured (curve)

3-body correlated wavefunction. Table 7.1 gives some other results for the liquid ^{4}He ground-state energy using various methods.

Detailed path integral Monte Carlo calculations have been performed on liquid ^{4}He [7.19, 75, 82, 92]. Figure 7.8 shows the comparison of the energy with experiment. It seems that PIMC can get energies accurate to 0.1 K except above the transition where rounding due to finite system effects occur. Path integral calculations for other properties at low temperatures agree well with GFMC results, and are in reasonable agreement with experiment. A particularly nice result is the calculated behaviour of the superfluid fraction as shown in Fig. 7.9.

7.4.2 ^{3}He Results

The ^{3}He Monte Carlo results are not nearly as accurate as those for ^{4}He. The fermi nature of ^{3}He makes even the ground-state energy difficult to calculate as described in Sect. 7.2 and in II. In Table 7.2, we show some results for the unpolarized liquid ^{3}He ground state. The 2-, 3-body and backflow correlated wavefunction produces the best variational results [7.93], although the pairing wavefunction of *Bouchaud* and *Lhuillier* [7.47] also gives a reasonable value. Unfortunately the pairing function used in that calculation has a large discontinuity at the edge of the simulation cell, thus the results are not necessarily upper bounds. The discontinuity introduces large additional size dependence that must be corrected for. Size dependence of the order of 0.1 K is a problem in all ^{3}He simulations as mentioned at the beginning of this chapter.

We also show in Table 7.2 fixed-node, approximate mirror potential, and a transient estimate result [7.21]. By comparison with experiment it appears

that the transient estimate result has converged. Unfortunately, the situation is not clear-cut due to differences in potentials, system sizes, estimation of errors, etc. It is still not clear precisely how good the various proposed nodes, trial functions, potentials, algorithms and methods for correcting for the finite sizes are for liquid ^{3}He at the level of 0.1 K. A satisfactory calculation of the energy of ^{3}He versus spin polarisation has not yet been completed.

7.4.3 Solid He

In the solid phase, the shadow form at a density of 0.0329 A^{-3}, gives an energy of -3.56 ± 0.03 K compared to a localised-Jastrow result of -3.32 ± 0.02 K and -3.79 ± 0.01 K when 3-body correlations are added [7.7]. PIMC calculations in the solid phase do not have symmetry breaking terms which are introduced with the localised trial functions in GFMC or VMC. PIMC calculations have been made of the quantum solid of hard spheres and of ^{4}He with the Aziz HFDHE2 and Lennard–Jones potential [7.71,94]. Elastic constants and the phase diagram of ^{4}He have also been extracted from these hard-sphere calculations [7.76,95,96].

The exchange frequencies of ^{3}He and ^{4}He atoms in the bulk solid have been calculated with PIMC [7.97]. It is found that pair interchange is most frequent, but that is followed closely by three and four atom exchange. The multiple exchange model [7.84] is strongly supported, but the calculations differ from that model in that a spectrum of exchanges is predicted to result in the experimental values of the magnetic ordering temperature and magnetic susceptibility. Even though the frequencies of some of the exchanges are small they are numerous. The importance of so many exchanges complicates the already difficult task of determining from the lattice Hamiltonian, the low temperature magnetic properties.

7.5 Momentum and Related Distributions

7.5.1 The Single-Particle Density Matrix

The single particle density matrix is

$$\rho_1(r_1, r_2) = \langle \psi^+(r_1)\psi(r_2) \rangle,$$

where the brackets indicate the thermodynamic average over the states of the system, and $\psi^+(r)$ is a creation operator for a particle at position r. For a system in a normalised eigenstate Ψ,

$$\rho_1(r_1, r_1') = N \int d^3r_2 \cdots d^3r_N \Psi^*(r_1, r_2, \ldots, r_N) \Psi(r_1', r_2, \ldots, r_N), \tag{7.69}$$

and for a system at inverse temperature β,

$$\rho_1(r_1, r_1', \beta) = N \int d^3r_2 \cdots d^3r_N \rho(r_1, r_2, \ldots, r_N; r_1', r_2, \ldots, r_N; \beta), \tag{7.70}$$

where $\rho(R, R', \beta)$ is the N-particle density matrix with the symmetry or antisymmetry required by bose or fermi statistics. Equation (7.70) is just the Boltzmann average of (7.69) over the states of appropriate particle statistics. These equations have tacitly assumed spin independence of the density matrix. For partially spin polarised systems, the density matrices of the spin up and spin down particles are calculated by choosing particle 1 in (7.69) or (7.70) to be spin up or down respectively, and the factor N is replaced by the number of up or down spins.

For homogeneous systems,

$$\rho_1(\boldsymbol{r}_1, \boldsymbol{r}_1') = \rho_1(|\boldsymbol{r}_1 - \boldsymbol{r}_1'|), \tag{7.71}$$

because of translational and rotational invariance. The fourier transform of $\rho_1(r)$ is the momentum distribution,

$$n(\boldsymbol{p}) = \langle a_{\boldsymbol{p}}^+ a_{\boldsymbol{p}} \rangle, \tag{7.72}$$

where $a_{\boldsymbol{p}}^+$ is a creation operator for a particle in a state of momentum $\boldsymbol{p}$. Typically, $n(p)$ is calculated by Fourier transforming ρ_1, and rather than enforce the periodicity of the simulation cell, the spherically averaged $\rho_1(r)$ is extrapolated smoothly to large r, and

$$n(\boldsymbol{p}) = N n_0 \delta_{\boldsymbol{p},0} + \int e^{-i\boldsymbol{p}\cdot\boldsymbol{r}} (\rho_1(r) - \rho n_0) d^3 r, \tag{7.73}$$

where n_0 is the condensate fraction, and ρ is the bulk density. The condensate fraction is directly given by the large r behaviour of ρ_1,

$$\lim_{r \to \infty} \rho_1(r) = \rho n_0. \tag{7.74}$$

The kinetic energy is

$$\frac{\langle p^2 \rangle}{2m} = \frac{\int d^3 p n(p) p^2}{2m \int d^3 p n(p)}, \tag{7.75}$$

and should agree with direct calculations. The kinetic energy is proportional to the curvature of $\rho_1(r)$ at $r = 0$.

Calculation of ρ_1 for bosons is conceptually quite simple with PIMC. One simply cuts one of the polymer chains and measures the end-to-end distribution of the two cut ends. The condensate fraction is the value of the distribution at large end-to-end separations, divided by its value at the origin. Thus condensation is equivalent to the unbinding of the two ends of a cut polymer. Hence, momentum condensation can only occur when a macroscopic polymer is present. Several tricks can be employed to achieve a more efficient estimation of this fraction. First, it is easy to estimate ρ_1 for small r by displacing an arbitrary atom from the diagonal simulation (no cut ends), and finding the change in the action. Second, when the ends are cut, one should apply importance sampling of the end-to-end distance so the errors coming from small distance approximately equal the errors from large distances. Third, one should preferentially move and permute the cut ends of the polymer. The computation of the momentum distribution in PIMC is inconvenient since a special calculation needs to be performed.

7.5.2 *y*-Scaling

The main interest in calculating $n(p)$ is to understand, approximately, the dynamic structure factor of quantum many-body systems. The impulse approximation for neutron scattering at large momentum transfers follows from the assumption that a neutron scatters off a single particle, and the outgoing wavefunction is a plane wave. At large momentum transfers, with soft potentials, *y*-scaling holds. That is, the scattering is proportional to the impulse approximation result, and the dynamic structure factor can be written as

$$S(\boldsymbol{k},\omega)=\frac{m}{q}n_0\delta(y)+\rho J(y), \tag{7.76}$$

where in the impulse approximation, $J(y)$ is

$$J_{\mathrm{IA}}(y)=\int n((y^2+p_p)^{1/2})\frac{d^2p_p}{(2\pi)^3}=\frac{1}{\pi}\int_0^\infty \rho_1(r)\cos(yr)dr, \tag{7.77}$$

and y is the *West* scaling variable [7.98], i.e. the longitudinal momentum transfer

$$y=\frac{m}{q}\left(\omega-\frac{q^2}{2m}\right). \tag{7.78}$$

The important result is that for large momentum transfers, $S(\boldsymbol{k},\omega)$ does not depend on $\boldsymbol{k}$ and ω independently, but only on y in $J_{\mathrm{IA}}(y)$. For hard-core potentials, final state effects modify the simple impulse approximation result [7.99–102]. *Silver* [7.101, 102] has given a simple prescription for including approximately final state effects by replacing $J_{\mathrm{IA}}(y)$ by a convolution of the longitudinal momentum distribution with a function that depends on the 2-body density matrix, with one particle diagonal and the other off-diagonal,

$$\rho_2(\boldsymbol{r}_1',\boldsymbol{r}_2,\boldsymbol{r}_1,\boldsymbol{r}_2)=\langle\psi^+(\boldsymbol{r}_1')\psi^+(\boldsymbol{r}_2)\psi(\boldsymbol{r}_1)\psi(\boldsymbol{r}_2)\rangle. \tag{7.79}$$

The main correction in this theory is therefore from an additional contribution from a spectator particle carrying off a portion of the momentum. Equation (7.79) is calculated straightforwardly using either PIMC or GFMC [7.94].

Carraro and *Koonin* [7.103] have recently studied final state effects in ^{4}He directly, using a variational wavefunction and the Monte Carlo method. Instead of assuming an outgoing plane wave as in the impulsive approximation, they explicitly solve for the outgoing wavefunction using the static positions of the spectator particles, sampled from a pair product trial function. The method therefore includes multiple scattering corrections to all orders. Because only the longitudinal component of the momentum is important, their method is computationally simple since only a 1D scattering problem needs to be solved for each independent set of sampled particle positions. Their derived effective final state broadening function becomes narrower at lower momentum transfers in contrast to Silver's result. Although they used a variational wavefunction, the incorporation of their method into a path integral or Green's function Monte Carlo calculation would be feasible.

7.5.3 Momentum Distribution Results

Momentum distributions have been calculated, for both ^{3}He and ^{4}He ground-states [7.18, 47] and for ^{4}He at finite temperatures [7.19, 94]. *Kalos* et al. [7.88] and *Whitlock* and *Panoff* [7.18] have calculated the momentum distribution of liquid and solid ^{4}He using GFMC. For the equilibrium density liquid, $\rho = 0.0218\,\text{A}^{-3}$, they obtain a ground-state condensate fraction of $9.2\% \pm 0.1\%$ as compared to the experimental estimate of $10\% \pm 2.0\%$ at $T = 1.5\,\text{K}$ [7.104]. The experimental estimate may be more uncertain than this, due to the extreme difficulty of pulling out the contribution of a delta function from inelastic neutron scattering cross sections which have been broadened by final state effects, instrumental resolution and multiple scattering. The GFMC condensate fraction decreases to $3.8\% \pm 0.2\%$ at $\rho = 0.0262\,\text{A}^{-3}$ [7.88]. An interesting variational result, using the shadow wavefunction, is a condensate fraction of $4.51\% \pm 0.03\%$ at equilibrium density [7.29]. This illustrates the difficulty of drawing firm conclusions about quantities (other than the energy) with the variational method, particularly in regards to long-range order.

Ceperley and *Pollock* [7.19] calculate a condensate fraction at SVP from $T = 1$–$4\,\text{K}$. They get a value of 8% with error bars of order $\pm 1\%$ between $T = 1\,\text{K}$ and $T = 2\,\text{K}$. The condensate fraction drops rapidly above 2 K as the system goes through its lambda point, with results consistent with no condensate, as expected, for temperatures greater than 3 K. Accurate estimation of the

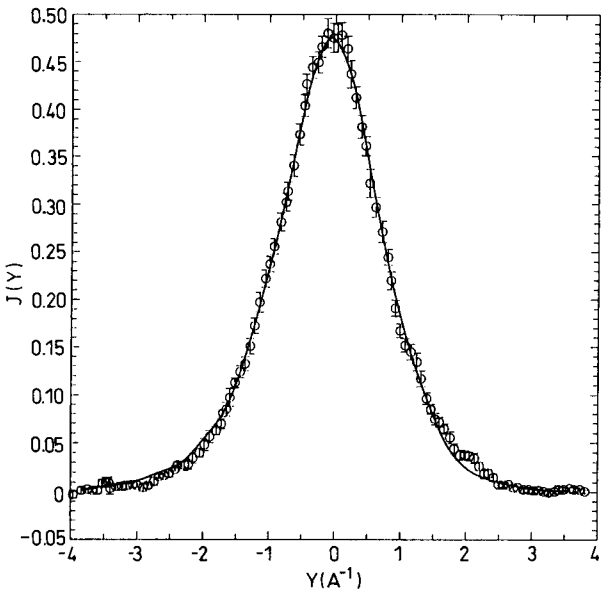

Fig. 7.10. The measured $J(y)$ of (7.76) at 0.32 K (circles) compared with the GFMC ground state result (solid line). The GFMC [7.18] result has been modified as described in the next. Data from *Sokol* et al. [7.105]

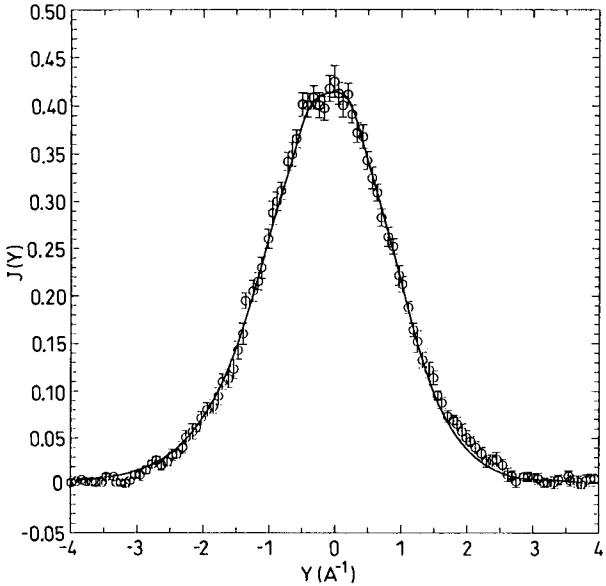

Fig. 7.11. The measured $J(y)$ of (7.76) at 3.33 K (circles) compared with the PIMC result (solid line) [75]. Data from *Sokol* et al. [7.105]

condensate fraction in the critical region requires simulations of much larger systems than have been used to date. At the higher density of $\rho = 0.0262\,\text{A}^{-3}$, PIMC predicts a condensate fraction of 2.6%.

In Figs. 7.10 and 11 we show results taken from [7.105] of the measured $J(y)$ along with the calculated $J(y)$ [7.18, 19] at two temperatures. The calculated $J(y)$ have been convoluted with an instrumentation resolution function, and the zero temperature GFMC results have been modified by convoluting with a final state effects function [7.101]. The results agree within experimental errors. Without the final state effect corrections to the GFMC results, the low temperature experiment and theory differ by about 10% at the peak of $J(y)$. *Carraro* and *Koonin* [7.103] calculate an equally good fit at these momentum transfers.

For Bose solids, the possibility of a condensate has not been thoroughly investigated. The importance functions used by *Whitlock* and *Panoff* [7.18] were of the localised form, and do not allow a condensate. At finite temperature one will have a condensate only if the two ends of a cut path become delocalised. Thus condensation is associated with the formation of bounded vacancy-interstitial pairs and with the existence of arbitrarily long ring exchanges. PIMC calculation find the exchange frequencies for three and four atom exchanges in solid ^{4}He are 1–4 μK. The low temperature and the small value of the expected condensate are discouraging. Recent calculations show that shadow trial wavefunctions do have a non-zero condensate in the solid [7.106], but numerical calculations have not extracted a non-zero value [7.29]. The $\rho_1(r)$ in the solid

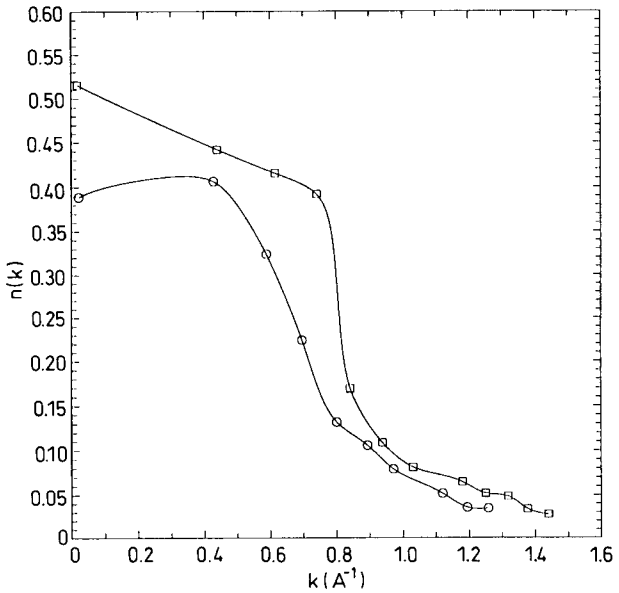

Fig. 7.12 The calculated ground-state momentum distribution of liquid ^{3}He at equilibrium density from fixed-node GFMC [7.18] (squares) and using the pairing wave function of *Bouchaud* and *Lhuillier* [7.47] (circles). The curves are drawn through the points only as a guide

phase is well represented by a gaussian; typically, the moments of ρ_1 deviate by only a few per cent from gaussian behaviour [7.29].

There are few experimental results for liquid ^{3}He and simulations are not as reliable as those for Bose systems. The momentum distributions for the ground-state of ^{3}He liquid have been calculated variationally and using fixed-node GFMC [7.18, 20, 47]. Shown in Fig. 7.12 is the momentum distribution at equilibrium density calculated variationally with the Bouchaud and Lhuillier pairing trial function and with fixed-node GFMC. The GFMC results has a fermi liquid discontinuity at the fermi momentum, but it is unlikely that this type of calculation can break away from the initial assumed symmetry of the model function, a perfect fermi gas. The Bouchaud and Lhuillier pairing form does not have a fermi surface. Unfortunately, final state effects may make ^{3}He neutron scattering experiments insensitive to this difference [7.102].

Sokol et al. report an experimental kinetic energy for ^{3}He at equilibrium density of $8.1^{+1.7}_{-1.3}$ K [7.107], while fixed-node GFMC calculations give 12.28 ± 0.04 K and transient estimates give 12.40 ± 0.10 K [7.21]. The discrepancy here is about 2.5 standard deviations. This may be due to any of the following: statistical errors, the difficulty of extracting the kinetic energy from the experimental neutron scattering, the GFMC extrapolation errors, the fixed-node approximation or lack of convergence of the transient estimation, or simulation size dependence.

7.6 Droplets and Surfaces

Although experimental results for small helium droplets are not yet available, clusters have been seen in rare gas jets [7.108, 109]. The main motivation of studying droplets is to obtain a better understanding of finite systems where physical boundary conditions can be handled exactly; to understand the transition from the finite system to the bulk limit; and to understand liquid-gas interfaces. In the future the same methods will be used to understand systems with pores and other restricted geometries [7.110].

7.6.1 Ground States of He Droplets

Calculations on ^{4}He droplets with N up to 728 were done by *Pandharipande* et al. [7.22, 111] using Green's function Monte Carlo and variational Monte Carlo. Their variational wavefunctions contained 2- and 3-body correlations as discussed in Sect. 7.1. However, for $N \leqq 10$ they find that their best variational

Table 7.3. The ground-state energy (in K) and radius (in A) for N atom ^{4}He droplets calculated with various methods. VMC1, VMC2 and VMC3 are the variational results of [7.111, 112, 23] respectively. GFMC is the Green's function Monte Carlo result from [7.22], and DMC is the diffusion Monte Carlo result from [7.23]. Energy error estimates are given in parenthesis. Where more than one energy is given, we have reported the results with the lowest variational value. The PIMC result [7.113] is at a temperature of 0.5 K. The last column is an estimate of the lowest energy excitation with zero angular momentum

N	Calculation	$E_0(K)$	r_0(A)	$E_E - E_0$(K)
3	GFMC	−0.0391(1)	5.35	
8	VMC1	−0.5989(8)	—	
8	GFMC	−0.6165(6)	3.19	
20	VMC1	−1.5734(13)	2.27	2.85(1)
20	VMC2	−1.514(3)	2.73	3.42
20	GFMC	−1.627(3)	2.71	
40	VMC1	−2.389(2)	2.54	2.79(4)
40	VMC3	−2.196(1)	2.63	
40	GFMC	−2.487(3)	2.57	
40	DMC	−2.529(3)	2.55	3.53
64	PIMC	−2.81(5)	2.46	
70	VMC1	−3.031(3)	2.48	2.75(15)
70	VMC2	−3.005(3)	2.42	4.22
70	GFMC	−3.12(4)	2.47	
70	DMC	−3.188(2)	2.44	3.91
112	VMC1	−3.498(5)	2.43	2.63(7)
112	VMC3	−3.143(2)	2.49	
112	GFMC	−3.60(1)	2.44	
112	DMC	−3.702(3)	2.40	3.92
240	VMC1	−4.193(5)	2.37	2.64(8)
240	VMC2	−4.192(4)	2.22	2.86
768	VMC1	−4.938(5)	2.32	
∞	Experiment	−7.14	2.22	0.0

results are obtained with the 2-body correlation chosen to have the asymptotic form

$$\lim_{r\to\infty} f(r) = e^{-\kappa r} r^{-1/(N-1)}, \tag{7.80}$$

which has the effect of holding the droplet together. For $N > 10$ they add a one-body correlation between each particle and the centre of mass of the droplet to bind the droplet. Similar calculations have been done recently by *Chin* and *Krotscheck* [7.23], who did variational and DMC calculations of droplets up to $N = 192$ and by *Rama Krishna* and *Whaley* [7.112] who have calculated, using variational Monte Carlo, droplets up to $N = 240$. These latter results used the newer HFDB potential of *Aziz* et al. [7.11] while the others used the HFDHE2 potential [7.8]. This must be taken into account when comparing their results. Chin and Krotscheck used a simple 2-body McMillan, $f(r) = \exp[-\frac{1}{2}(b/r)^5]$, correlation and a gaussian 1-body factor for their importance function. Rama Krishna and Whaley used a wavefunction similar to that of *Pandharipande* et al.

In Table 7.3 we have collected ground-state energies per particle and unit radii, defined to be $\sqrt{(5/3)} r_{\rm rms} N^{-1/3}$, where $r_{\rm rms}$ is the root mean square radius from the centre of mass, for droplets up to $N = 768$. We see that there is reasonable agreement, but discrepancies between the GFMC and DMC results, particular at $N = 112$, may indicate lack of convergence. The variational results using the HFDHE2 potential (VMC1) also are remarkably close to those using the HFDB potential (VMC2). The density profiles of the droplets are much harder to calculate due to statistical errors and slow convergence of the GFMC and DMC methods. The result of Pandharipande et al. and Rama Krishna and Whaley show results consistent with a smooth profile. Chin and Krotscheck show a small oscillatory structure in their DMC density profiles for $N > 70$ which persists for large numbers of iterations. Similar oscillations were seen earlier by Pandharipande et al. In both calculations, large initial oscillations die out. It is not clear how much, if any, of this structure will remain in a completely converged calculation. Some of these effects may also be caused by the extrapolation from the mixed and variational estimates. The PIMC results at finite temperature [7.113] do not have this problem of extrapolation (but are at finite temperature though a superfluid has few excitations) and do not show the same structure as Chin's density profile.

Pandharipande et al. have fit their GFMC energies and those of the bulk [7.88] as

$$\frac{E}{N}(K) = -7.10 + 17.6x + 1.15x^2 - 30.6x^3 + 19.5x^4, \tag{7.81}$$

where $x = N^{-1/3}$. Taking the derivative and assuming a liquid drop radius, they extract a surface tension of $0.28\,\mathrm{K\,A^{-2}}$ as compared to an experimental values of $0.274\,\mathrm{K\,A^{-2}}$ [7.114] and $0.265\,\mathrm{K\,A^{-2}}$ [7.115].

7.6.2 Excitations in Droplets

All three groups have calculated an upper bound to the low energy excitations of ^{4}He droplets using the Feynman excitation operator method [7.116]. They assume the excited state wavefunction can be approximated by

$$\Psi_E = \sum_i \chi(r_i - r_{cm})\Psi_0 = F\Psi_0,$$

where Ψ_0 is the exact ground-state wavefunction, and r_{cm} is the centre of mass of the droplet. χ is a function to be determined variationally. A bound on the excited state energy E_E is written as

$$E_E - E_0 = \frac{1}{2}\frac{\langle \Psi_0 | [F,[T,F]] | \Psi_0 \rangle}{\langle \Psi_0 | F^2 | \Psi_0 \rangle}, \tag{7.82}$$

where T is the kinetic energy operator. Equation (7.82) is the ratio of two ground-state expectation values and can be written in terms of ground-state distribution functions. Typically, χ is expanded is spherical harmonics and (7.82) minimised, subject to the constraint that Ψ_E is orthogonal to the lower energy states, to obtain approximate excited state wavefunctions.

The calculations of *Pandharipande* et al. [7.111] and *Rama Krishna* and *Whaley* [7.112] have used the variational wavefunction as an approximation to the ground state, while Chin and Krotscheck have used their DMC results for the distribution functions. A comparison of some excitation energies of the lowest angular momentum zero states are shown in Table 7.3. We see that there is qualitative agreement, but little quantitative agreement between the calculations. Calculations of other states have been done by each of these groups. The results of Chin and Krotscheck are probably the most reliable, because of their use of the diffusion Monte Carlo ground-state wavefunction. Calculations with backflow correlations in the excitation operator are more difficult, and have not yet been done, but would presumably give better excitation energies.

7.6.3 ^{3}He Droplets

The ground states of ^{3}He droplets have been studied by *Pandharipande* et al. [7.111] and *Lewart* et al. [7.117] using variational Monte Carlo and wavefunctions containing 2-body, 3-body, and backflow correlations of the type described in Sect. 7.1. They fit their variational ^{3}He energies to polynomials of the form of (7.81). Their results indicate that the 20 particle droplet is not bound, but is in a metastable state. The 20 particle droplet was found to be unbound in an earlier fixed-node GFMC calculations [7.118]. Fixed-node Green's function Monte Carlo calculations indicate that the 70 particle variational energy is only about 0.1 K too high per particle. The single particle density shows shell structure expected in a fermi droplet.

Lewart et al. calculate the single particle density matrix (see Sect. 7.5) of both ^{4}He and ^{3}He droplets using variational Monte Carlo. They also define and calculate the quasi-particle wavefunctions defined by

$$\phi_{qp}(r_1) \alpha \int \Psi_h^*(R)\Psi_0(R) d^3r_2 \cdots d^3r_N \tag{7.83}$$

where Ψ_h is a single hole state of $N-1$ particles, and is approximated by omitting a particle and an orbital from the model function. For bulk systems, the orbitals in the Slater determinant, the quasiparticle wavefunctions, and the natural orbitals, ψ_i, defined by diagonalising the single particle density matrix,

$$\rho_1(r'_1, r_1) = \sum_i n_i \psi_i^*(r_1)\psi_i(r'_1) \tag{7.84}$$

are all plane waves. For droplets these functions are all distinct, and related to different excitation properties. The n_i in (7.84) are the analog of the momentum distributions, and n_0 is the generalisation, in a droplet, of the condensate fraction.

7.6.4 Droplets at Finite Temperature

Helium-4 droplets of 64 and 128 atoms have been studied at temperatures below 2 K [7.113]. The specific heat shows a broadened transition from the normal liquid to the superfluid as expected. The normal (i.e. non-superfluid) density is defined as the ratio of the moment of inertia of the droplet to its classical value defined in terms of the radius of gyration as discussed in Sect. 7.3.10. The superfluid density is then calculated as proportional to the mean squared area swept out by a path. Most of the droplet becomes superfluid below 1.5 K. The density profiles are in reasonable agreement with those calculated with GFMC.

7.6.5 Surfaces and Interfaces

Helium adsorbed on substrates can be simulated directly once a helium-substrate potential is assumed. One approximation for monolayer systems is to assume that the substrate strongly binds the helium, and view the monolayer as a 2D film. A number of calculations have been done on 2D helium atoms at both zero and finite temperatures [7.0, 119–122]. *Whitlock* et al. [7.119] have found that the liquid ^{4}He freezes at a density of $0.0678\,\text{A}^{-2}$ and melts at a density of $0.0721\,\text{A}^{-2}$ at zero temperature. The zero pressure, zero temperature density of the liquid is $0.04356\,\text{A}^{-2}$. At this density the condensate fraction is approximately 0.25, much larger than in 3-dimensions due to the reduced interatomic spacing.

The PIMC method has also been applied to 2D helium [7.92]. At zero temperature, the 2D and 3D systems are similar, but at any non-zero temperature the 2D system is described by the Kosterlitz–Thouless picture of a vortex unbinding transition. According to this theory, the single particle density matrix decays algebraically with a temperature dependent power, instead of to a constant as it does in 3D. In addition, the superfluid density should jump from zero at high temperature to a finite value at the critical temperature. These effects are what are observed in the simulations, although finite-size scaling is needed to understand the rounding that occurs in a simulation of a finite system. At a density of $0.0432\,\text{A}^{-2}$, the superfluid transition is predicted by the PIMC calculations to occur at a temperature of 0.72 K. The vortex diameter and the core energy is estimated to be 3.7 A and 2.7 K respectively.

Approximating the effective two-body potential in a monolayer as the bare potential is equivalent to assuming that the atomic separations in the monolayer are much greater than the thickness of the layer. A somewhat better approximation can be made by assuming a substrate potential, and using its ground state to define the layer profile and the effective interaction in the 2D system. However, for a model graphite substrate, the effect on the energy difference is only about 0.05 K per particle [7.123]. A discussion of some other effects of the 2D approximation is given by *Cheng* and *Cole* [7.124].

The surface tension and surface profile has been calculated for a self-bound slab of ^{4}He by *Valles* and *Schmidt* [7.24]. They get a value for the surface tension of $0.265\,\mathrm{K\,A^{-2}}$ as compared to an experimental values of $0.274\,\mathrm{K\,A^{-2}}$ [7.114] and $0.265\,\mathrm{K\,A^{-2}}$ [7.115], and the value, given above, extracted from droplet data of $0.28\,\mathrm{K\,A^{-2}}$.

An area where much further work needs to be done is the calculation of the properties of helium on realistic substrates. An interesting calculation studying the registered phases of a monolayer of ^{3}He on graphite is given by *Abraham* and *Broughton* [7.125] using a PIMC. *Abraham* et al. [7.126] have studied with VMC and PIMC, the detailed structure of two solid players of ^{3}He on graphite in an attempt to understand the unusual phase transitions that occur at this density. They find that the proposed $\sqrt{7} \times \sqrt{7}$ registered structure is stable at low temperatures and melts at approximately 1 K.

7.7 Future Prospects

GFMC and PIMC methods have given us the ability to calculate from first principles, properties of many-body boson systems, at zero and non-zero temperature with computable errors. What are some of the challenging problems given that the basic equilibrium situation for bosons is in good shape? Some of the obvious applications for many-boson systems yet to be investigated are bosons in disordered environments or on surfaces, impurities in helium, and the study of excitations such as vortices, rotons and maxons.

One of the major unsolved problems in computational physics is to devise a method to simulate large many-fermion systems without uncontrolled approximations. The auxiliary field (Stratonovich–Hubbard transformation) method does just that for the Hubbard model at half filling on a bipartite lattice. For general models, the most successful ground state methods use a fixed-node approximation, but the bias introduced by the trial nodes restricts the applicablity of the method to systems where the long-range order is well understood. Currently the path integral fixed-node method is under investigation for the simulation of fermion continuum systems at finite temperature. One chooses a trial density matrix and throws out walks which cross the nodes of the trial density matrix. If the nodes are chosen correctly then the method is exact. This method will be useful at temperatures larger than the fermi energy

where the nodes are closely related to the classical nodes, and goes over smoothly to the ground state fixed-node method. Again it is only applicable if the long-range structure of the density matrix is understood. Thus the fermion simulation problem, to calculate the properties of a many-body fermion systems in time which is a power of the number of fermions and the inverse temperature, is very largely unsolved.

A second major unsolved problem is to calculate dynamical properties of quantum systems. To calculate general dynamical properties seems very difficult. Even specifying the initial conditions would require an exponentially large amount of data. Luckily, most interesting questions come down to equilibrium dynamics in the linear response regime. In PIMC one can easily compute imaginary time correlation functions. The problem is to rotate it back into real time. A simple example is the dynamical density–density response function, $S(k, \omega)$. Its Laplace transform can be calculated in either DMC or PIMC as

$$F(k,t) = \langle \rho_k(0)\rho_{-k}(t)\rangle = \int_{-\infty}^{\infty} d\omega e^{-\omega t} S(k,\omega),$$

where $\rho_k(t)$ means the phonon operator (7.20) evaluated at imaginary time t. However the inversion to obtain S from F is numerically unstable. Recently maximum entropy methods [7.127] have been applied to this inversion procedure with some success for lattice models. These methods combine highly accurate Monte Carlo generated imaginary time response functions with any theoretical input that may be available, and effectively give the most likely dynamical response function consistent with all the available data. We anticipate that the method will have broad application in understanding equilibrium dynamics of quantum systems.

Acknowledgements. DMC is supported by the National Science Foundation through grant number NSF DMR88-08126 and the department of physics at the University of Illinois. KES is supported by the National Science Foundation through grant number NSF CHE90-15337.

References

7.1 D.M. Ceperley, M.H. Kalos: In *Monte Carlo Methods in Statistics Physics*, Topics Curr. Phys. Vol. 7, ed. by K. Binder (Springer, Berlin, Heidelberg 1979)
7.2 K.E. Schmidt, M.H. Kalos: In *Monte Carlo Methods in Statistical Physics II*, Topics Curr. Phys. Vol. 36, ed. by K. Binder (Springer, Berlin, Heidelberg 1984)
7.3 S.C. Pieper, R.B. Wiringa, V.R. Pandharipande: Phys. Rev. Lett. **64**, 365 (1990)
7.4 J. Carlson: Phys. Rev. C **36**, 2026 (1987)
7.5 J. Carlson: Phys. Rev. C **38**, 1879 (1988)
7.6 J.P. Bouchaud, C. Lhuillier: Europhys. Lett. **3**, 1273 (1987)
7.7 S. Vitiello, K.J. Runge, M.H. Kalos: Phys. Rev. Lett. **60**, 1970 (1988)
7.8 R.A. Aziz, V.P.S. Nain, J.S. Carley, W.L. Taylor, G.T. McConville: J. Chem. Phys. **70**, 457 (1974)

7.9 D.M. Ceperley, H. Partridge: J. Chem. Phys. **84**, 820 (1986)
7.10 R. Feltgen, H. Kirst, K.A. Köhler, H. Pauly, F. Torello: J. Chem. Phys. **76**, 2360 (1982)
7.11 R.A. Aziz, F.R.W. McCourt, C.C.K. Wong: Mol. Phys. **61**, 1487 (1987)
7.12 B. Liu, A.D. McLean: J. Chem. Phys. **91**, 2348 (1989)
7.13 P.A. Whitlock, D.M. Ceperley, G.V. Chester, M.H. Kalos: Phys. Rev. B **19**, 5598 (1979)
7.14 B.M. Axilrod, E. Teller: J. Chem. Phys. **11**, 293 (1943)
7.15 R.E. Lowther, R.L. Coldwell: Phys. Rev. A **22**, 14 (1980)
7.16 V. Mohan, J.B. Anderson: In *Quantum Simulations of Condensed Matter Phenomena*, ed. by J.D. Doll, J.B. Gubernatis (World Scientific, Singapore 1990)
7.17 G.J. Tawa, P.A. Whitlock, J.W. Moskowitz, K.E. Schmidt: to be published in Int. J. Sup. Appl. (1990)
7.18 P.A. Whitlock, R.M. Panoff: Can. J. Phys. **65**, 1409 (1987)
7.19 D.M. Ceperley, E.L. Pollock: Can J. Phys. **65**, 1416 (1987)
7.20 D.M. Ceperley, M.H. Kalos, G.V. Chester: Phys. Rev. B **16**, 3081 (1977)
7.21 R.M. Panoff, J. Carlson: Phys. Rev. Lett. **62**, 1130 (1989)
7.22 V.R. Pandharipande, J.G. Zabolitzky, S.C. Pieper, R.B. Wiringa, U. Helmbrecht: Phys. Rev. Lett. **50**, 1676 (1983)
7.23 S.A. Chin, E. Krotscheck: Phys. Rev. Lett. **65**, 2658 (1990)
7.24 J.L. Valles, K.E. Schmidt: Phys. Rev. B **38**, 2879 (1988)
7.25 K. Binder, D.W. Heermann: In *Monte Carlo Simulation in Statistical Physics*, Topics Curr. Phys. Vol. 7 (Springer, Berlin, Heidelberg 1988)
7.26 K. Binder, D. Stauffer: In *Monte Carlo Methods in Statistical Physics II*, Topics Curr. Phys. Vol. 36, ed. by K. Binder (Springer, Berlin, Heidelberg 1984)
7.27 N. Metropolis, A.W. Rosenbluth, H. Rosenbluth, A. Teller, E. Teller: J. Chem. Phys. **21**, 1087 (1953)
7.28 R.P. Feynman, M. Cohen: Phys. Rev. **102**, 1189 (1956)
7.29 S. Vitiello, K.J. Runge, G.V. Chester, M.H. Kalos: Phys. Rev. **42**, 228 (1990)
7.30 E. Saunders: Phys. Rev. **126**, 1724 (1962)
7.31 L.H. Nosanow: Phys. Rev. Lett. **13**, 270 (1964)
7.32 L.H. Nosanow: In *Quantum Solids and Fluids*, ed. by S.B. Trickey, E.D. Adams, J.W. Duffy (Plenum, New York 1977)
7.33 D. Ceperley, G.V. Chester, M.H. Kalos: Phys. Rev. B **17**, 1070 (1978)
7.34 R.M. Panoff: In *Condensed Matter Theories* (Plenum, New York 1987)
7.35 R.A. Aziz, P.K. Pathria: Phys. Rev. A **7**, 827 (1972)
7.36 P.R. Roach, S.B. Ketterson, C.-W. Woo: Phys. Rev. A **2**, 543 (1970)
7.37 C.-W. Woo: Phys. Rev. Lett. **29**, 1442 (1972)
7.38 C.C. Chang, C.E. Campbell: Phys. Rev. B **15**, 4238 (1977)
7.39 V.R. Pandharipande: Phys. Rev. B **18**, 218 (1978)
7.40 K.E. Schmidt, V.R. Pandharipande: Phys. Rev. B **19**, 2504 (1979)
7.41 K.E. Schmidt, M.H. Kalos, M.A. Lee, G.V. Chester: Phys. Rev. Lett. **45**, 573 (1980)
7.42 D. Levesque, C. Lhuillier: Phys. Rev. B **23**, 2203 (1981)
7.43 Q.N. Usmani, S. Fantoni, V.R. Pandharipande: Phys. Rev. B **26**, 6123 (1982)
7.44 K.E. Schmidt, J.W. Moskowitz: J. Chem. Phys. **93**, 4172 (1990)
7.45 M.P. Allen, D.J. Tildesley: *Computer Simulation of Liquids* (Oxford University Press, Oxford 1987)
7.46 J.P. Bouchaud, C. Lhuillier: J. Physique (Paris) **49**, 553 (1988)
7.47 J.P. Bouchaud, C. Lhuillier: In *Spin Polarised Quantum Systems*, ed. by S. Stringari (World Scientific 1989)
7.48 J. Bardeen, L.N. Cooper, J.R. Schrieffer: Phys. Rev. **108**, 1175 (1957)
7.49 T. Muir: *A Treatise on the Theory of Determinants* (Dover, New York 1960)
7.50 W. Wu, S.A. Vitiello, L. Reatto: To be published in the *Proceedings of the Elba International Physics Center* (Giardini, Rome 1990)
7.51 W. Wu, S.A. Vitiello, M.H. Kalos: Submitted to Phys. Rev. Lett. (1990)
7.52 W.G. Stirling: In *Proceedings of the second international conference on phonon physics*, ed. by J. Kollar (World Scientific, Philadelphia, 1985), p. 829
7.53 O.W. Dietrich, E.H. Graf, C.H. Huang, L. Passel: Phys. Rev. A **5**, 1377 (1972)
7.54 C.J. Umrigar, K.G. Wilson, J.W. Wilkins: Phys. Rev. Lett. **60**, 1719 (1988)
7.55 C.J. Umrigar, K.G. Wilson, J.W. Wilkins: In *Computer Simulation Studies in Condensed Matter Physics: Recent Developments*, ed. by D.P. Landau, K.K. Mon, H.B. Schuttler (Springer, New York 1988)

7.56 K.E. Schmidt, S. Vitiello: In *Condensed Matter Theories* (Plenum, New York 1989)
7.57 B. Bernu, D.M. Ceperley, V.W. Laster, Jr.: J. Chem. Phys. **93**, 552 (1990)
7.58 E. Feenberg: *Theory of Quantum Fluids* (Academic, New York 1969)
7.59 V.R. Pandharipande, H.A. Bethe: Phys. Rev. C 7(4), 1312 (1973)
7.60 K.E. Schmidt: In *Models and Methods in Few-Body Physics*, ed. by A. Fonseca, Lecture Notes in Physics (Springer, Berlin, Heidelberg 1987)
7.61 S. Chin: Texas A and M preprint (1989)
7.62 M.H. Kalos, J. Carlson: Phys. Rev. C **32**, 1735 (1985)
7.63 R.L. Stratonovich: Sov. Phys. Dokaldy **2**, 416 (1957)
7.64 J. Hubbard: Phys. Rev. Lett. **3**, 77 (1959)
7.65 G. Sugiyama, S.E. Koonin: Ann. Phys. **168**, 1 (1986)
7.66 S.B. Fahy, D.R. Hamann: Phys. Rev. Lett. **65**, 3437 (1990)
7.67 W. Wu, S. Vitiello, K.J. Runge, MH. Kalos: Preprint (1990)
7.68 S. Vitiello, K.J. Runge, in *Computer Simulation Studies in Condensed Matter Physics: Recent Developments*, Eds. D.P. Landau, K.K. Mon, H.B. Schuttler (Springer, Berlin, Heidelberg 1988)
7.69 R.P. Feynman: *Statistical Mechanics* (Addison-Wesley, Reading 1972)
7.70 L.D. Landau, E.M. Lifshitz: *Statistical Physics* (Addision-Wesley, Reading 1969)
7.71 E.L. Pollock, D.M. Ceperley: Phys. Rev. B **30**, 2555 (1984)
7.72 J.A. Barker: J. Chem. Phys. **70**, 2914 (1979)
7.73 A.D. Klemm, R.G. Storer: Aust. J. Phys. **26**, 43 (1973)
7.74 D.M. Ceperley, E.L. Pollock: Path-Integral Computation Techniques for Superfluid 4He, to be published in *Proceedings of the Workshop on Monte Carlo Methods in Theoretical Physics, Isla D'Elba, Italy*, ed. by S. Fanstoni, Giordini Publishing, 1991
7.75 D.M. Ceperley, E.L. Pollock: Phys. Rev. Lett. **56**, 351 (1986)
7.76 K. Runge, G.V. Chester: Phys. Rev. B **38**, 135 (1988)
7.77 J.D. Doll, R.D. Coalson, D.L. Freeman: Phys. Rev. Lett. **55**, 1 (1985)
7.78 M. Takahashi, M. Imada: J. Phys. Soc. Jpn. **53**, 963 (1984)
7.79 M. Sprik, M.L. Klein, D. Chandler: Phys. Rev. B **31**, 4234 (1985)
7.80 E.J. Brushkin, M.F. Herman, B.J. Berne: J. Chem. Phys. **76**, 5150 (1982)
7.81 M. Parrinello, A. Rahman: J. Chem. Phys. **80**, 860 (1984)
7.82 E.L. Pollock, D.M. Ceperley: Phys. Rev. B **36**, 8343 (1987)
7.83 G.G. Batrouni, R.T. Scalettar, G.T. Zimanyi: Phys. Rev. Lett. **65**, 1765 (1990)
7.84 M. Roger, J. Hetherington, J.M. Delrieu: Rev. Mod. Phys. **55**, 1 (1983)
7.85 M.C. Cross, D.S. Fischer: Rev. Mod. Phys. **57**, 881 (1985)
7.86 C.H. Bennett: J. Comput. Phys. **22**, 245 (1976)
7.87 B.J. Berne, D. Thirumalai: Ann. Rev. Phys. Chem. **37**, 401 (1986)
7.88 M.H. Kalos, M.A. Lee, P.A. Whitlock, G.V. Chester: Phys. Rev. B **24**, 115 (1981)
7.89 P.A. Whitlock, K.E. Schmidt, M.A. Lee: unpublished
7.90 D.O. Edwards, R.C. Pandroff: Phys. Rev. (1981) A **140**, 816 (1965)
7.91 V.F. Sears, E.C. Svensson, A.D.B. Woods, P. Martel: *Atomic Energy of Canada Limited Report No. AECL-6779* (unpublished)
7.92 D.M. Ceperley, E.L. Pollack: Phys. Rev. B **39**, 2084 (1989)
7.93 K.E. Schmidt, M.A. Lee, M.H. Kalos, G.V. Chester: Phys. Rev. Lett. **47**, 807 (1981)
7.94 D.M. Ceperley: In *Momentum Distributions*, ed. by R.E. Silver, P.E. Sokol (Plenum Press, New York 1989)
7.95 K.J. Runge, G.V. Chester: Phys. Rev. B **39**, 2707 (1989)
7.96 A. Meroni, L. Reatto, K.J. Runge: In *Condensed Matter Theories* (Plenum, New York 1989)
7.97 D.M. Ceperley, G. Jacucci: Phys. Rev. Lett. **58**, 1648 (1987)
7.98 G.B. West: Phys. Rept. **18C**, 263 (1975)
7.99 V.F. Sears: Phys. Rev. B **30**, 44 (1984)
7.100 J.J. Weinstein, J.W. Negele: Phys. Rev. Lett. **49**, 1016 (1982)
7.101 R.N. Silver: Phys. Rev. B **38**, 2283 (1988)
7.102 R.N. Silver: In *Momentum Distributions*, ed. by R.E. Silver, P.E. Sokol (Plenum Press, New York 1989)
7.103 C. Carraro, S.E. Koonin: Phys. Rev. Lett. **65**, 2792 (1990)
7.104 H.A. Mook: Phys. Rev. Lett. **51**, 1454 (1983)
7.105 P.E. Sokol, T.R. Sosnick, W.M. Snow: In *Momentum Distributions*, ed. by R.E. Silver, P.E. Sokol (Plenum Press, New York 1989)
7.106 L. Reatto, G.L. Masserini: Phys. Rev. B **38**, 4516 (1988)

7.107 P.E. Sokol, K. Sköld, D.L. Price, R. Kleb: Phys. Rev. Lett. **54**, 909 (1985)
7.108 J. Fargo, M.F. de Feraudy, B. Raoult, G. Torchet: J. Physique (Paris), Colloq. **38**, C2 (1977)
7.109 O. Echt, K. Saltler, E. Rechnagel: Phys. Rev. Lett. **47**, 1121 (1981)
7.110 F.M. Gasparini, I. Rhee: to be published in *Prog. in Low Temp. Phys.* Vol. **XIII** (1990)
7.111 V.R. Pandharipande, S.C. Pieper, R.B. Wiringa: Phys. Rev. B **34**, 4571 (1986)
7.112 M.V. Rama Krishna, K.B. Whaley: J. Chem. Phys. **93**, 746 (1990)
7.113 P. Sindzingre, M.L. Klein, D.M. Ceperley: Phys. Rev. Letts. **63** 1601 (1989)
7.114 H.M. Guo, D.O. Edwards, R.E. Sarwinski, J.T. Tough: Phys. Rev. Lett. **27**, 1259 (1971)
7.115 M. Iino, M. Suzuki, A.J. Ikushima: J. Low Temp. Phys. **61**, 155 (1985)
7.116 R.P. Feynman: Phys. Rev. **94**, 262 (1954)
7.117 D.S. Lewart, V.R. Pandharipande, S.C. Pieper: Phys. Rev. B **37**, 4950 (1988)
7.118 K.E. Schmidt: In *Monte Carlo Methods in Quantum Problems*, Proceedings of the NATO-ARW, ed. by M.H. Kalos (Reidel, Dordrecht 1984)
7.119 P.A. Whitlock, G.V. Chester, M.H. Kalos: Phys. Rev. B **38**, 2418 (1988)
7.120 T.C. Padmore: Phys. Rev. Lett. **32**, 826 (1974)
7.121 K.S. Liu, M.H. Kalos, G.V. Chester: Phys. Rev. B **13**, 1971 (1976)
7.122 X.-Z. Ni, L.W. Bruch: Phys. Rev. B **33**, 4584 (1986)
7.123 P.A. Whitlock, K.E. Schmidt: to be published
7.124 E. Cheng, M.W. Cole: Submitted to Phys. Rev. B (1990)
7.125 F.F. Abraham, J.Q. Broughton: Phys. Rev. Lett. **59**, 64 (1987)
7.126 F.F. Abraham, J.Q. Broughton, P.W. Leung, V. Elser: Europhys. Lett. **12**, 107 (1990)
7.127 R.N. Silver, D.S. Sivia, J.E. Gubernatis: Phys. Rev. B **41**, 2380 (1990)